Volume 57
Number 74
21 September 2021
Pages 9305–9476

ChemComm

Chemical Communications

rsc.li/chemcomm

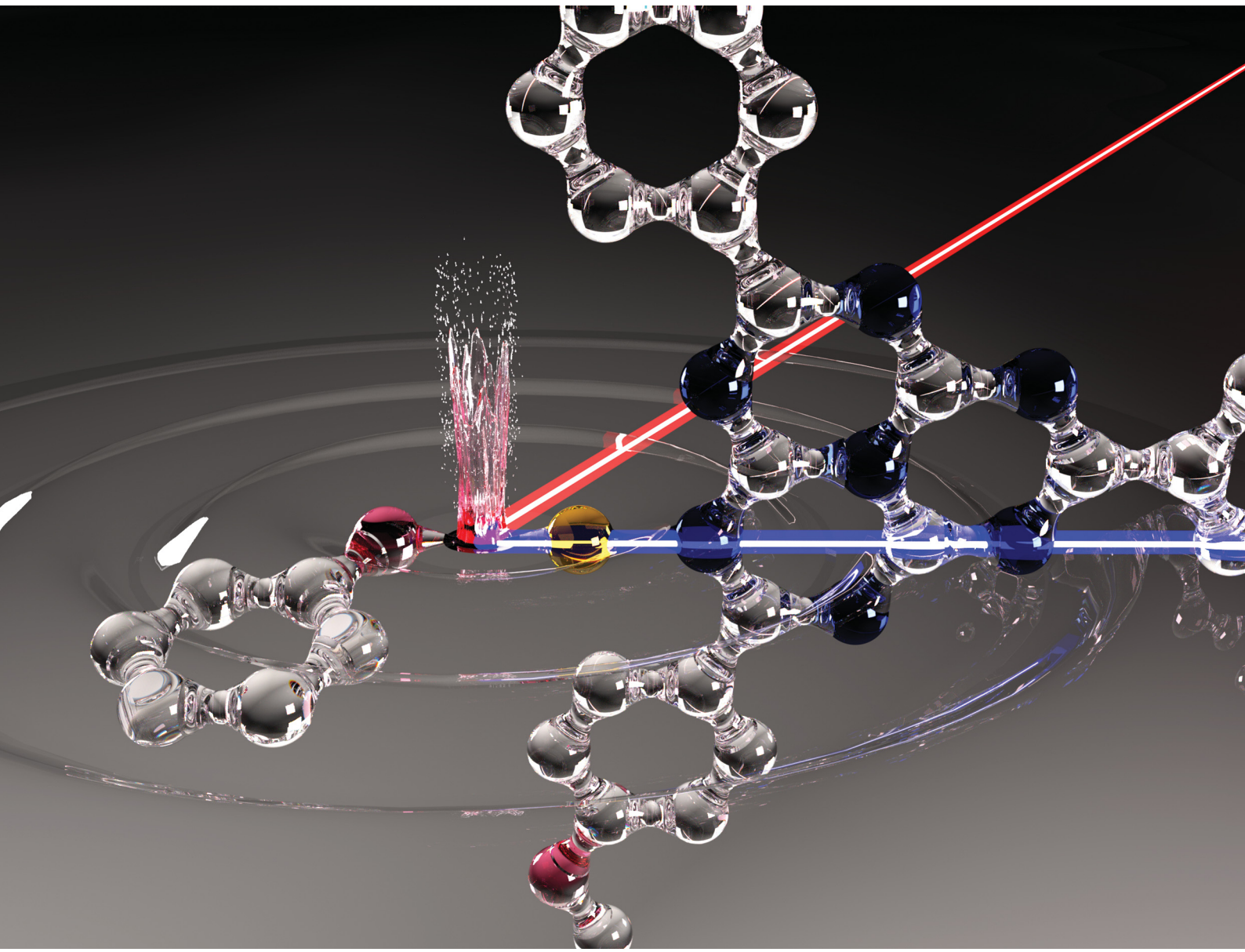

ISSN 1359-7345

ROYAL SOCIETY OF CHEMISTRY

FEATURE ARTICLE

Doyk Hwang and Cody W. Schlenker

Photochemistry of carbon nitrides and heptazine derivatives

ChemComm

ROYAL SOCIETY OF CHEMISTRY

FEATURE ARTICLE

View Article Online
View Journal | View Issue

Cite this: *Chem. Commun.*, 2021, **57**, 9330

Photochemistry of carbon nitrides and heptazine derivatives

Doyk Hwang [a] and Cody W. Schlenker *[abc]

We explore the photochemistry of polymeric carbon nitride (C_3N_4), an archetypal organic photocatalyst, and derivatives of its structural monomer unit, heptazine (Hz). Through spectroscopic studies and computational analysis, we have observed that Hz derivatives can engage in non-innocent hydrogen bonding interactions with hydroxylic species. The photochemistry of these complexes is influenced by intermolecular $n\pi^*/\pi\pi^*$ mixing of non-bonding orbitals of each component and the relative energy of intermolecular charge-transfer (CT) states. Coupling of the former to the latter appears to facilitate proton-coupled electron transfer (PCET), resulting in biradical products. We have also observed that Hz derivatives exhibit an extremely rare inverted singlet/triplet energy splitting (ΔE_{ST}). In violation of Hund's multiplicity rules, the lowest energy singlet (S_1) is stabilized relative to the lowest triplet (T_1) electronic excited state. Exploiting this unique inverted ΔE_{ST} character has obvious implications for transformational discoveries in solid-state OLED lighting and photovoltaics. Harnessing this inverted ΔE_{ST}, paired with light-driven intermolecular PCET reactions, may enable molecular transformations relevant for applications ranging from solar energy storage to new classes of non-triplet photoredox catalysts for pharmaceutical development. To this end, we have explored the possibility of optically controlling the photochemistry of Hz derivatives using ultrafast pump–push–probe spectroscopy. In this case, the excited state branching ratios among locally excited states of the chromophore and the reactive intermolecular CT state can be manipulated with an appropriate secondary "push" excitation pulse. These results indicate that we can predictively redirect chemical reactivity with light in this system, which is an avidly sought achievement in the field of photochemistry. Looking forward, we anticipate future opportunities for controlling heptazine photochemistry, including manipulating PCET reactivity with a diverse array of substrates and optically delivering reducing equivalents with, for example, water as a partial source of electrons and protons. Furthermore, we wholly expect that, over the next decade, materials such as Hz derivatives, that exhibit inverted ΔE_{ST} character, will spawn a significant new research effort in the field of thin-film optoelectronics, where controlling recombination *via* triplet excitonic states can play a critical role in determining device performance.

Received 25th May 2021,
Accepted 16th August 2021

DOI: 10.1039/d1cc02745j

rsc.li/chemcomm

Introduction

An immense research effort has been expended to understand fundamental photochemical processes involving organic chromophores. On the one hand, insights gained from such studies can be of potential relevance for sustainable energy technologies, such as solar energy storage,[1–4] on the other, they can aid in developing preparative photoredox catalysts for chemical synthesis.[5–9] While the sun has the capacity to provide ample energy to satiate immediate and future global power demands, its intermittency compels improvements in the overall cost, efficiency, and scalability of solar capture, conversion, and storage strategies.[10,11] Nevertheless, catalytically driving chemical reactions to store solar energy remains a challenging problem and an increasingly attractive goal.[12] There are numerous areas of reaction chemistry that would be desirable to drive with light, most prominent among these is arguably the splitting of water to generate hydrogen and oxygen.[13–17] Other potential applications, may focus on photocatalytically generating, otherwise elusive, high-energy intermediates, such as amidyl radicals for synthesizing pharmaceuticals and other value-added products,[6,18] or reactive oxygen species for remediating polluted water.[19,20] These processes often involve complex kinetic barriers, which can, in principle, be traversed with PCET steps that require the coordinated motion of multiple electrons and multiple protons.[21–25] Much of the

[a] *Department of Chemistry, University of Washington, Seattle, Washington 98195, USA*
[b] *Molecular Engineering & Sciences Institute, University of Washington, Seattle, Washington 98195-1652, USA*
[c] *Clean Energy Institute, University of Washington, Seattle, Washington 98195-1653, USA. E-mail: schlenk@uw.edu*

fundamental kinetics of these subtle and highly complex photochemical systems remain poorly understood and difficult to control. One common case involves the hydrogen and oxygen evolution reactions, where a murky understanding of the reaction kinetics appears to have stunted progress toward development and technological implementation of viable photocatalytic systems utilizing solar radiation.[13,16,26]

Various strategies for tackling the water splitting problem exist, from conventional photovoltaic-electrolysis (PV-E) to photoelectrochemical (PEC) cells and photocatalyst suspensions.[27] While a suspension-based approach seems conceptually simple, the PV-E and PEC approaches enjoy substantial advantages for immediate implementation, including well-developed knowledge and infrastructure from existing technology. Practical solar-to-hydrogen (STH) efficiency limits for these more established technologies have been estimated to be roughly 32% at 1 Sun irradiation.[28] Devices with STH efficiencies approaching these limits have been demonstrated at laboratory scale with PV-E[29] architectures. Similarly, devices based on PEC[30] architectures with STH efficiencies approaching the thermodynamic limit for a particular bandgap have also been demonstrated. However, technoeconomic analysis suggests that the levelized cost of hydrogen (LCH) produced by panel-based PV-E would be roughly three to five times higher than that predicted for photocatalytic systems and, indeed, uncompetitive against production from fossil sources.[12,31] As an alternative, some have postulated that suspension-based approaches with photocatalytic particles could potentially benefit from industrial plant designs with completely new form factors, with the potential to produce hydrogen at costs closer to current market prices.[31] However, there are far more technological and scientific unknowns, not to mention market risks, associated with such approaches.[12,32] Not least of these is the obvious practical challenge of separating H_2 and O_2 products. Nevertheless, there have been numerous attempts to develop novel, efficient, inexpensive, and robust photocatalyst materials for the purpose of driving solar water splitting. These have ranged from semiconductor nanoparticles[33,34] to organic-based and polymeric photocatalysts.[35–37] The perceived potential for low-cost and scalability has recently made organic photocatalysts an attractive platform. However, the challenges and uncertainties noted above for photocatalytic systems imply that, on some level, the value of such demonstrations may ultimately be rooted less in their direct technological significance and more in the fundamental insight that may be gleaned from these photochemical and electrochemical reactivity studies. Nevertheless, such new insight may foster new light-driven reaction chemistries or even hybrid energy storage devices, such as surface functionalized photoactive electrodes with heightened activity. For example, light-driven accumulation of two redox equivalents on surface-bound arylamines has recently been demonstrated on functionalized TiO_2 particles.[38] Given that it has long been recognized that such bipolaronic states form readily in many organic semiconductors,[39–42] it seems plausible that surface-bound systems capable of exploiting the accumulation of multiple redox equivalents may be of general significance to photocatalysis.

One specific motivating factor behind a relatively intense recent research effort focused on organic-based materials for photocatalysis stems from the development of various polymeric carbon nitride (C_3N_4) materials over the past decade.[43–49] Polymeric C_3N_4 exists in multiple forms, including poly-triazines and poly-heptazines; among those compositions, the most commonly studied subject is arguably graphitic C_3N_4 (g-C_3N_4), comprising two dimensional sheets of heptazine (Hz) units (Fig. 1A).[50] The g-C_3N_4 variant has several desirable characteristics, including facile synthesis from common precursors and comparatively robust photochemical stability. It has also been shown that g-C_3N_4 has photocatalytic activity toward various reactions, ranging from water splitting and hydrogen evolution[51] to carbon dioxide reduction,[52]

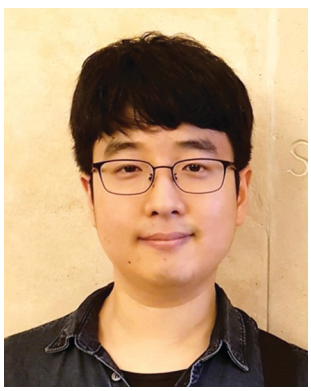

Doyk Hwang

Doyk Hwang obtained BS (2012) and PhD (2018) in Chemistry from the Seoul National University (Republic of Korea) under the supervision of Professor Seong Keun Kim, where he studied photoactive molecules and materials with femtosecond spectroscopy. In 2019, he joined Professor Xiaoyang Zhu's group at Columbia University as a postdoctoral researcher, studying photonic-excitonic couplings of perovskites. In 2020, he joined Professor Cody W. Schlenker's group at the University of Washington. His research interests are focused on understanding fundamental mechanism of metal-free photocatalysts and improving their properties.

Cody W. Schlenker

Cody W. Schlenker is the Washington Research Foundation Innovation Assistant Professor in Chemistry and Clean Energy at the University of Washington in Seattle. Dr Schlenker earned his BS in Chemistry from Linfield College (2004) and PhD in Chemistry from the University of Southern California (2010) studying molecular optoelectronics. After his doctorate, Dr Schlenker studied photophysics of semiconducting polymers at University of Washington as an NSF SEES Fellow. Professor Schlenker joined the UW Department of Chemistry faculty in 2014, where his research group focusses on solar energy conversion and storage processes in photovoltaics, photocatalysts, photon upconversion systems, and rechargeable batteries.

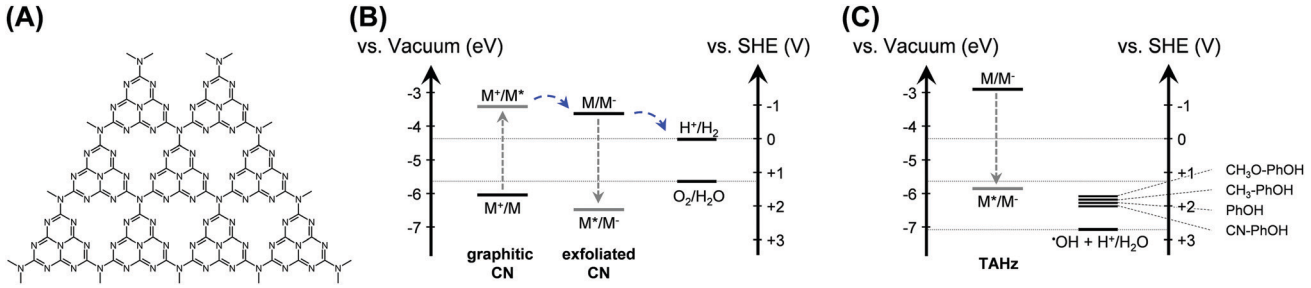

Fig. 1 (A) Idealized molecular structure of graphitic Carbon Nitride (g-C_3N_4). (B) Experimentally measured redox potential and calculated excited-state redox potential from optical gap of g-C_3N_4, exfoliated C_3N_4, and (C) the monomeric Hz derivative 2,5,8-tris(4-methoxyphenyl)-1,3,4,6,7,9,9*b*-heptaazaphenalene (TAHz). Oxidation potential of g-C_3N_4 and reduction potential of exfoliated C_3N_4 and TAHz are measured by cyclic voltammetry (CV) with FTO working electrode, Ag/AgCl reference electrode, and Pt counter electrode. For g-C_3N_4 and exfoliated C_3N_4, CV was performed in sodium hydroxide (0.5 M, aq) with C_3N_4/Nafion matrix coated FTO electrode. For TAHz, CV was performed with 475 μM TAHz in THF with 250 mM $TABPF_6$. Excited state redox potential was calculated with optical gap (S_0-S_1) determined from absorption and photoluminescence spectroscopy. For reference, half-reaction redox potentials of $2H^+(aq)|H_2(g)$, $O_2(g) + 4H^+(aq)|H_2O(l)$, $^\bullet OH(aq) + H^+(aq)|H_2O(l)$, and R-$PhOH^+$|R-PhOH (in acetonitrile) are presented. Blue dashed arrows in (B) represent a viable electron transfer cascade pathway from photoexcited graphitic C_3N_4 to aqueous hydronium ion, resulting in H_2 evolution (see below). Adapted with permission from ref. 93 and 102. Copyright 2019 and 2017 American Chemical Society.

degradation of chemical pollutants,[53] and olefin hydroamidation.[54,55] Numerous chemical modifications of g-C_3N_4 have been applied to explore its photocatalytic activity. For example, Zhu and coworker applied chemical exfoliation to bulk g-C_3N_4 and observed an increase in their H_2 production rate of ~2.6 times, which they attributed to increased surface area.[56] Lau *et al.* showed chemical modifications that introduced oxygen containing terminal groups improved hydrogen generation efficiency.[57] Other works have focused on modifying morphology,[58] changes in crystallinity,[59] fragmentation of g-C_3N_4,[60] and metal ion doping.[61]

Lotsch and coworkers have taken a synthetic approach to evaluating the activity of polymeric C_3N_4 variants, in conjunction with computational analysis and experimental characterization, including X-ray diffraction, IR and NMR spectroscopy, mass spectrometry, and electron microscopy. Their work suggested that specific functional groups, such as the cyanamide moiety, support higher catalytic activity, which they surmised was due to enhanced coordination with a Pt co-catalyst.[57,62] The same group has also noted that different counter cations may influence activity by modulating inter-plane stacking.[63] Durrant and coworkers have taken a spectroscopic approach, using steady-state and femtosecond time-resolved spectroscopy to study excited-state dynamics in several g-C_3N_4 varients.[64] From these results, they concluded that photoinduced electron accumulation occurred in their cyanimide-functionalized materials when paired with an appropriate sacrificial electron donor.[65] The authors in that work noted a correlation between their observed kinetic spectroscopy measurements and redox reaction mechanisms, and concluded that excessive electron accumulation limits the H_2 production rate by accelerating charge recombination.[66] Antonietti and coworkers have surveyed a range of C_3N_4 morphologies and chemical functionalization. Modifications such as co-condensation and shortening interlayer distance,[67] introducing nanostructured geometries,[68] or increasing structural flexibility,[69] appear to increase the oscillator strength of formally symmetry-forbidden low-energy Hz transitions. Many other studies have focused on leveraging the symmetry-forbidden, weak nπ* transition that extends into the visible region to improve the spectral response of C_3N_4 at longer wavelengths.[70–73] Other groups have employed quantum chemical calculations, such as recent surface hopping and nonadiabatic quantum dynamics simulations,[74–77] to evaluate plausible photochemical pathways for C_3N_4 photocatalysis.

However, the preponderance of previous work has focused on g-C_3N_4 materials in the context of their potential semiconductor photophysics, such as bandgap and exciton dynamics.[78–82] By comparison, analysis of catalytic activity of g-C_3N_4 based on its molecular monomers and their photochemical properties has received far less attention, with only a few reported results.[62,83–86] However, the ever-present structural heterogeneity and diverse chemical composition of g-C_3N_4 materials makes it extremely difficult to conduct systematic analysis of their photoactivity. To the best of our knowledge, there have been no reports demonstrating pure ballistic charge transport in carbon nitrides. While charge generation, likely at interlayer defect sites, has been observed spectroscopically on rapid, sub-picosecond timescales, photon absorption appears to initially produce bound excitons in these materials. For example, based on detailed photoluminescence analysis, Merschjann and coworkers concluded that 2-D Hz-based C_3N_4 behave electronically as optical quasi-monomers, rather than classical wide band gap covalent crystalline semiconductors.[87] Domcke, Sobolewski and coworkers studied a molecular mechanism of C_3N_4 photocatalysis from *ab initio* computational analysis, suggesting that a photochemical reaction of the Hz moiety and water may be active in C_3N_4.[88] Contrast this with the photoinduced electron transfer processes that are widely studied for proton reduction by semiconductor photocatalysts. This analysis suggests that the language of local molecular orbital interactions may lead to fruitful mechanistic insight regarding the photochemical reactivity of g-C_3N_4. Nevertheless, a common lexicon to describe material properties can be a unifying force in a multidisciplinary arena. We adopt a nomenclature that we have discussed previously,[89–91] which is based on the oxidizing and reducing potentials of the ground or

excited electronic states, rather than on the nature of their charge transport characteristics, be they band-like, hopping, or otherwise. Using this excited state potential framework, the driving force for photoinduced charge transfer of C_3N_4 can be compared against classic semiconductors, polymers, or molecules with minimal confusion.

Fig. 1B and C show ground and excited state redox potentials of g-C_3N_4, chemically exfoliated C_3N_4, and the anisole-functionalized Hz monomer derivative, TAHz, compared with redox potentials of the hydrogen or oxygen evolution and the one-electron oxidation reactions for various hydroxylic species.[92,93] Based upon the corresponding thermochemical landscape, one anticipates that, upon photoexcitation, bulk g-C_3N_4, chemically exfoliated C_3N_4 flakes, and TAHz could all be capable of photochemically generating hydrogen or oxygen from water. However, as shown in numerous previous research with C_3N_4 and other catalytic systems, there exist other aspects that are critical for determining the overall photocatalytic efficiency.[46] One important, widely accepted bottleneck in the water splitting reaction is the kinetically-limited four-electron transfer process of oxygen evolution reaction.[15–17] Alternatively, there has been significant interest recently in photocatalytically generating $^{\bullet}OH$ or H_2O_2, as well as using water as a source of electrons and protons for running photocatalytic reduction reactions.[94–97]

Pairing ultrafast spectroscopy measurements with *ab initio* quantum chemical calculations has recently revealed the role of H-bonding interactions as one critical element for supporting photoinduced intermolecular PCET reactions, resulting in homolytic O–H bond cleavage. Domcke, Sobolewski, and coworkers have explored H-bond formation of Hz monomers in g-C_3N_4 with water and excited state PCET processes resulting in water oxidation using *ab initio* calculations and compared these results with well-known N-heterocyclic molecules such as pyridine and triazine.[85,88] A similar PCET-induced water oxidation reaction was also observed by Zhang and coworkers from excited state nonadiabatic dynamics simulation showing ultrafast electron-driven proton transfer from water to Hz,[75] and also by Bande and coworkers from their excited state electron dynamics calculation with nitrogen-doped C_3N_4-like graphene oxides.[98] Notably, these studies generally indicate that the traditional electrochemical potentials used to estimate reaction free energies such as those presented in Fig. 1B and C, for bulk g-C_3N_4, chemically exfoliated C_3N_4 flakes, and a monomeric Hz derivative do not adequately represent the photochemical reactivity of the hydrogen bonded complex. Rather, one-electron water oxidation is facilitated through the PCET process and the thermodynamically favorable but kinetically cumbersome four-electron transfer process is avoided.[84,99,100]

As we describe in this Feature Article, one of our goals has been to reveal new insight into the fundamental photochemistry of heptazine-based materials by spectroscopically examining the kinetics of the excited-state reaction chemistry in which they engage. Among several findings that our work has uncovered, the following are particularly noteworthy: (1) intermolecular hydrogen bonding interactions result in new excited states, which appear to serve as a gateway to hole transfer from hydroxylic species; (2) this hole transfer can be predictably controlled using tunable laser pulse sequences; (3) the intermolecular hydrogen bonding interaction appears to influence excited state deformations of the chromophore, which may modulate these photon-driven reactions; and (4) the intriguing photophysical and photochemical behavior of heptazine derivatives is, in part, due to a rather unique inversion of its lowest-energy singlet and triplet excited states that results from a combination of spin polarization effects and the orthogonality of their HOMO and LUMO orbitals.

Mechanistic study of carbon nitride photocatalyst

I. Ultrafast electron transfer and reactivity enhancement in polymeric carbon nitrides

Among the numerous studies regarding the catalytic activity of g-C_3N_4 photocatalysts, several have found that specific chemical modifications of g-C_3N_4, including introducing defects[101] or oxidative terminations[57] in bulk g-C_3N_4 enhance performance of photocatalysis. In particular, adding chemically exfoliated C_3N_4 flakes with more termination sites improves catalytic activity and hydrogen production rates of bulk g-C_3N_4 by $\sim$2.3 times, even without a Pt co-catalyst.[60] Based on these experimental observations, our group initially focused on a heterogeneous g-C_3N_4 catalyst platform blended with exfoliated C_3N_4. This effort centered on revealing the underlying dynamic processes associated with this catalytic efficiency enhancement and clarifying the fundamental photocatalytic reaction mechanism of C_3N_4 catalysts. Fig. 2A shows preparation routes for g-C_3N_4 and exfoliated C_3N_4.[102] Briefly, g-C_3N_4 powder was treated with a highly-oxidizing mixture of sulfuric and nitric acids under ultrasonication and stirring. After 24 hours, the resulting mixture was treated with deionized water and filtered through a 0.45 μm PVDF mesoporous membrane. This process introduced oxidized termination sites and also shortened the π-conjugation length of the resulting heptazine-based material. These properties were explored using the experimental characterization tools described below. Based upon results from our X-ray photoelectron spectroscopy (XPS), FT-IR spectroscopy, and X-ray diffraction studies, the exfoliated C_3N_4 evidently differs from the parent bulk material in that it possesses substantially more oxidized chain terminations than bulk g-C_3N_4, which may serve as photochemical reaction sites. However, X-ray diffraction indicates that some degree of periodicity among Hz units is still maintained following the exfoliation process.[102] Consistent with the shorter π-conjugation length resulting from an increase in the number of chain terminations, exfoliated C_3N_4 exhibited a blue-shifted optical energy gap, observable in both the steady-state absorption and photoluminescence spectra (Fig. 2B). The optical energy gap, combined with electrochemical characterization, allow us to consider the energy levels for charge transfer, shown in Fig. 1B. These energy level estimates indicate that electron transfer from photoexcited g-C_3N_4 to our chemically exfoliated C_3N_4 material is an exergonic process. Interestingly, incorporating a small amount (10% by mass) of exfoliated C_3N_4 into a g-C_3N_4 suspension significantly enhances the catalytic activity of g-C_3N_4 (Fig. 2C),

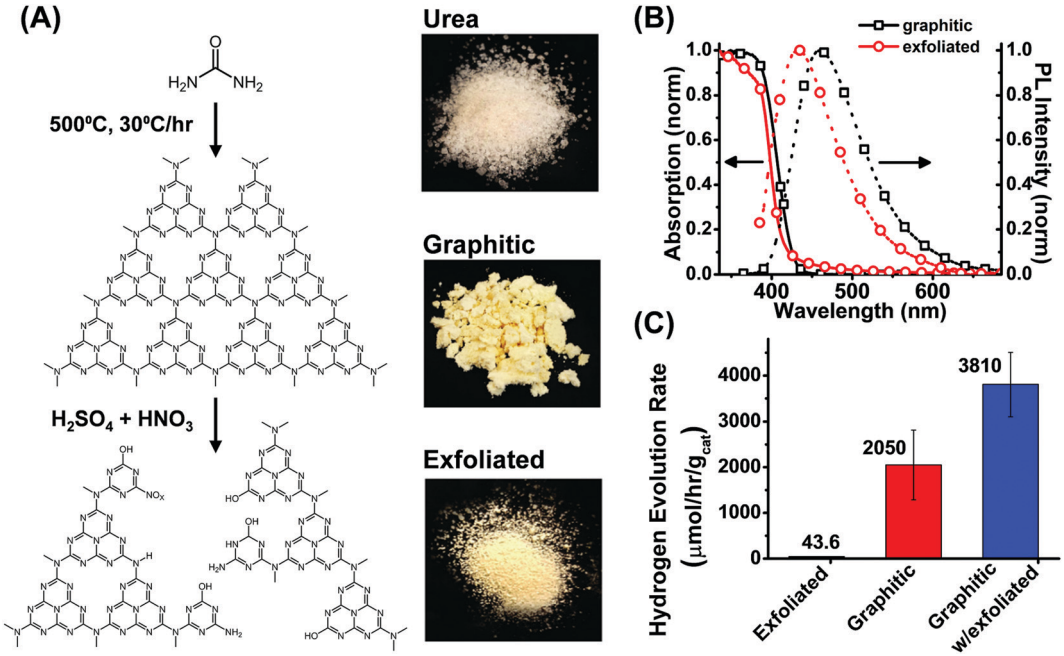

Fig. 2 (A) Schematic diagram for synthesis of g-C_3N_4 from Urea and chemical exfoliation of g-C_3N_4 into exfoliated flakes. (B) Ground-state absorption (solid lines) and steady-state luminescence spectra (dotted lines) for 365 nm excitation of graphitic (black) and exfoliated (red) C_3N_4 suspensions in deionized water. (C) Hydrogen activity for exfoliated C_3N_4, g-C_3N_4 and a g-C_3N_4 suspension infused with 10% mass-loading of exfoliated C_3N_4 co-catalyst under 365 nm LED illumination (21 mW cm^{-2}). Rates are for 2% Pt loading with 10% triethanolamine used as a sacrificial hole scavenger. Reprinted with permission from ref. 102. Copyright 2017 American Chemical Society.

this despite exfoliated C_3N_4 alone being virtually inactive toward H_2 production.

Photogenerated excitons and charge carriers, the primary participants in most photochemical and photophysical processes, are typically transferred on rapid timescales from femtoseconds to microseconds.[103] As a result, conventional steady-state characterization methods often fail to provide sufficient mechanistic information about the excited state species that drive photocatalytic reactions. Accordingly, we have utilized ultrafast spectroscopic techniques, including femtosecond transient absorption (TA) spectroscopy, in order to thoroughly probe photoinduced dynamics in the g-C_3N_4 mixed with exfoliated C_3N_4. As indicated in Fig. 3, global target analysis reveals that two different species contribute to the overall TA signal in the NIR probe range of the spectra for the g-C_3N_4 and blend samples. In global target analysis, we assume that experimental TA data consists of the superposition of species-associated difference spectra (SADS), weighted by a time-dependent concentration profile for each contributing species.[104,105] By comparing each SADS from our TA experiments with differential absorption spectra from cathodic spectroelectrochemical measurements,[102] we concluded that the two SADS recovered from our target analysis were attributable to photogenerated electrons and holes in g-C_3N_4, as shown in Fig. 3. This assignment was corroborated by control experiments wherein electron or hole scavengers were added to the sample.[102]

As shown in Fig. 3, adding exfoliated C_3N_4 flakes drastically quenches the photogenerated g-C_3N_4 electron signal but produces a negligible effect on the hole decay kinetics. The accelerated decay constant of photogenerated electron in g-C_3N_4 is about 660 ps, which is on the same order of diffusion-limited quenching. Since the concentration of exfoliated C_3N_4 is substantially lower than g-C_3N_4 in the blend sample (~10% by mass), these results indicate that the electrons initially photogenerated in g-C_3N_4 are rapidly transferred to exfoliated C_3N_4 and the catalytic enhancement primarily occurs at the exfoliated C_3N_4 containing the oxidized chain termination sites. This hypothesis is also supported by prior experimental observations[60] that adding small amounts of exfoliated C_3N_4 flakes drastically enhances catalytic activity of bulk g-C_3N_4. The enhanced catalytic activity upon adding chemically exfoliated g-C_3N_4 particles is consistent with previous structure–activity studies of carbon nitrides. These results indicated that introducing structural defects and increasing the number of chemically activated g-C_3N_4 chain termination sites, such as highly oxidized terminal groups, improves catalytic activity.[106–109] Based on these findings, we anticipated that heptazine oligomers or even monomers, may serve as viable photocatalysts and may exhibit compelling photochemistry in their own right.[110]

II. Proton-coupled electron transfer in monomeric heptazine photocatalysts

The monomeric heptazine unit of g-C_3N_4 (Fig. 1), has garnered significant research interest from the energy storage community.[62,88,111,112] This is, in part, due to the observations described above suggesting that exfoliated C_3N_4 can improve catalytic activity, but also from a fundamental standpoint as a testbed to better understand photon-driven chemical

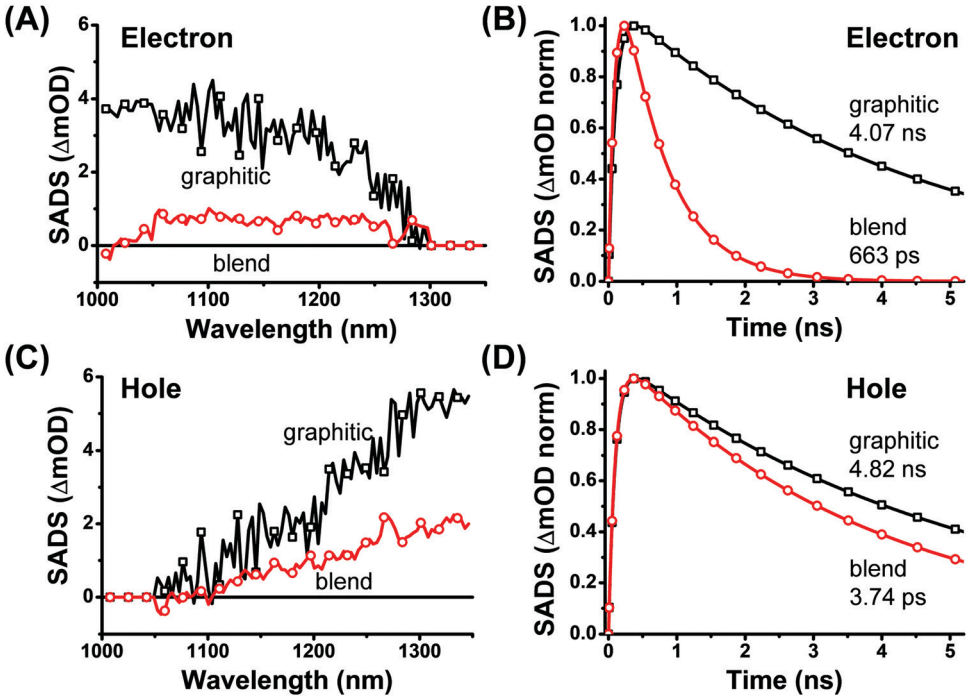

Fig. 3 Global target analysis of the femtosecond transient absorption data for g-C_3N_4 and a mixture of g-C_3N_4 plus 10% exfoliated C_3N_4 by mass ("blend") in deionized water. Species associated difference spectra (SADS), σ_e for the electron (A) and σ_h for the hole (C), correspond to the kinetics profiles in (B) and (D), respectively. The data used for this analysis were collected without platinum loading and in the absence of charge scavengers. Reprinted with permission from ref. 102. Copyright 2017 American Chemical Society.

transformations, such as H-atom abstraction, in greater detail.[84] We synthesized TAHz using Friedel–Crafts chemistry as a stable, well-defined, model Hz derivative (Fig. 4). We investigated its photophysical and photochemical properties in the presence of various hydroxylic compounds that are capable of hydrogen bonding with the nitrogen atoms on the perimeter of the heptazine core.[113]

Fig. 4A depicts one potential hydrogen bonding motif between heptazine derivatives and water *via* the peripheral nitrogen atoms of the heptazine rings. This hydrogen bonding interaction has been predicted by *ab initio* quantum chemical calculations to help facilitate intermolecular PCET reactions from H_2O to TAHz, leading to TAHz-H$^\bullet$ and $^\bullet$OH biradical products.[88] These theory-based results suggest that heptazine hydrogen bonding interactions with hydroxylic species, such as water, result in intermolecular complexes wherein new excited states with charge-transfer (CT) character from the Hz core to the oxygen p-orbital are formed. These intermolecular electronic states are distinct from the local ππ* and nπ* excited states associated with the isolated chromophore. The trace marked with blue filled circles in the right portion of the energy diagram in Fig. 4B illustrates that these CT states become energetically stabilized along the H-atom transfer coordinate. They can be regarded as a photochemical reaction pathway. Thus, excitation into the CT state can engender a PCET reaction, breaking the chemical bond between hydrogen and oxygen and transferring the H atom (electron + proton) to the heptazine core. In the subsequent sections of this Feature Article, we will outline a number of experimental observations reported by our group that are consistent with the theoretical framework described above for the photochemical reactivity of heptazine derivatives.

Electronic excited states of TAHz in the near UV to visible wavelength range mainly consist of an exceptionally bright, high-energy ππ* state and a low-lying, symmetry-forbidden ππ* state, with contributions from dark nπ* states of intermediate energy. From computational analysis, we attribute the intense absorption peak near 360 nm to the bright ππ* transition, while the much weaker absorption signatures near 450 nm and photoluminescence peak proximal to 510 nm are associated with a formally symmetry-forbidden ππ* transition. In the absence of hydrogen bonding with an external H-atom donor, initial excitation of the TAHz through the bright ππ* transition quickly results in nonradiative relaxation to the lowest dark ππ* excited state, which then can emit green fluorescence. However, with H-atom donors such as water, photoexcitation can initiate PCET reactions, as well as H_2 evolution (Fig. 4E). The PCET reaction was also probed by a drastic quenching of fluorescence lifetime of TAHz in water compared to that in toluene, and the $^\bullet$OH radical generation was detected by various methods, such as terephthalic acid adduct fluorescence[113] and spin-trapping EPR.[84] Interestingly, we see an H_2 production rate per mass catalyst from TAHz that is roughly on par with bulk g-C_3N_4 under otherwise identical conditions.[102]

In order to probe dynamics of the TAHz:H_2O complex and better understand the kinetics of this PCET reaction, we employed time-resolved PL (TR-PL) spectroscopy paired with global target analysis. While the overall emission spectral line shapes in toluene and water appear to be somewhat similar,

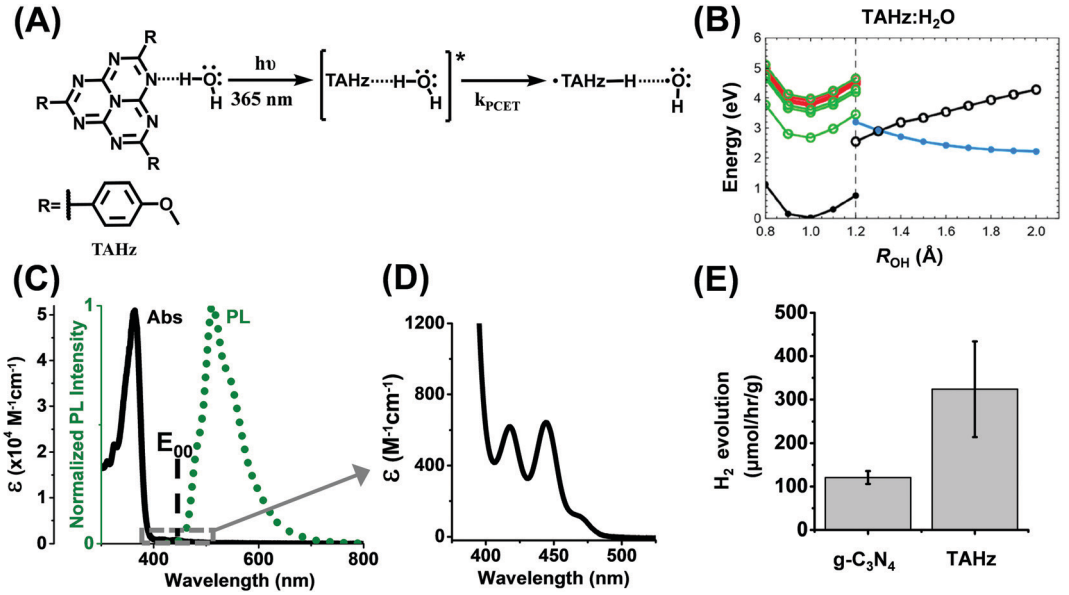

Fig. 4 Fig. 4 (A) Molecular structure of TAHz and proposed mechanism of PCET reaction with water. (B) *Ab initio* potential energy profiles of relaxed scans for the H-atom transfer reaction from water to TAHz. For $R_{OH} < 1.2$ Å, electronic ground state (black) was optimized, while for $R_{OH} > 1.2$ Å the charge-transfer state (blue) was optimized. ππ* states are shown in green, nπ* states are shown in red. (C) Absorption and photoluminescence spectrum of TAHz in toluene (33 μM). (D) Absorption spectrum of weakly allowed transitions around 400–500 nm below bright ππ* transition at 365 nm. (E) H_2 evolution rate for 3 mg TAHz, 15 mL of H_2O, 1.5 mL of triethanolamine, and 2 wt% Pt under 5 mW cm^{-2}, 365 nm LED illumination. H_2 activity of bulk g-C_3N_4 under identical conditions included for reference. Reprinted with permission from ref. 113 and 147. Copyright 2018 and 2020 American Chemical Society.

there are striking kinetic differences in the fluorescence that are revealed by analyzing the blue-edge (high-energy, short-wavelength region) of the emission envelope (Fig. 5A). Comparing decay kinetics at short and long wavelengths of this signal showed that there exist at least two different emitting species for the TAHz in water case. By contrast, we only observe one single emitting species in toluene, which is attributable to the S_1 excited state of free TAHz. We were able to resolve two different emission spectra contributing to the TR-PL data of TAHz in water using global analysis. These results reveal a new high-energy emission spectrum with shorter average lifetime, in addition to the low-energy spectrum that is attributable to free TAHz.

Since excited state PCET processes involve physical movement of a proton, one common way to characterize such a reaction is to deuterate the participating protic component, which, in many cases, can substantially decelerate the reaction kinetics.[114,115] When we changed the solvent from H_2O to D_2O, we observed a considerable kinetic isotope effect (KIE) in the PL lifetime of the high-energy emitting species, increasing by a factor of 2.9 (Fig. 5D). This result is consistent with H-atom transfer quenching of the luminescence as a result of the PCET reaction. On the other hand, the low-energy emitting species did not exhibit a substantial KIE upon deuteration, as expected for free TAHz undergoing collisional quenching. These results indicate that TAHz can form hydrogen bonded complexes with water that undergo photon-driven PCET reactions, resulting in one-electron homolytic water oxidation reactions to generate biradical products, as well as liberating H_2.

In this Feature Article, we cover two primary photoactivity modes for heptazine-based photocatalysts. One operating by reducing a substrate (*i.e.*, electron transfer to protons). The other operating by oxidizing a substrate (*i.e.*, PCET from water to the chromophore). Sacrificial reducing agents, which are often used in consort with metal co-catalysts, preferentially steer the photocatalytic activity toward proton reduction, masking any underlying activity toward water oxidation. For example, photoexcited TAHz will oxidize pure water by abstracting a hydrogen atom from it. However, we have shown that feeding photoexcited TAHz with triethanolamine as a sacrificial electron donor in an aqueous environment will cause TAHz to preferentially reduce protons instead.[113] Results from Kang and coworkers indicate that a composite of metal-free polymeric g-C_3N_4 and carbon nanodots, without any sacrificial reducing agent, supports photocatalytic water splitting by a two-electron water oxidation pathway, generating H_2 and O_2 *via* a peroxide intermediate.[116] More recent theory studies, employing tools such as nonadiabatic quantum dynamics simulations, have suggested that this overall water oxidation process is initiated by an excited-state PCET event that transfers an H-atom from water to the peripheral nitrogens in the heptazine ring of polymeric g-C_3N_4.[76,77] The substrate oxidation process described in those theoretical and experimental reports is consistent with the ''PCET from substrate'' reactivity that we observe for molecular heptazine derivatives, such as TAHz.[75,84] In the following sections, we focus on a model system to further explore the excited-state PCET reactivity of TAHz with functionalized phenols, to reveal more systematic control of molecular properties and a deeper understanding of the excited states involved.

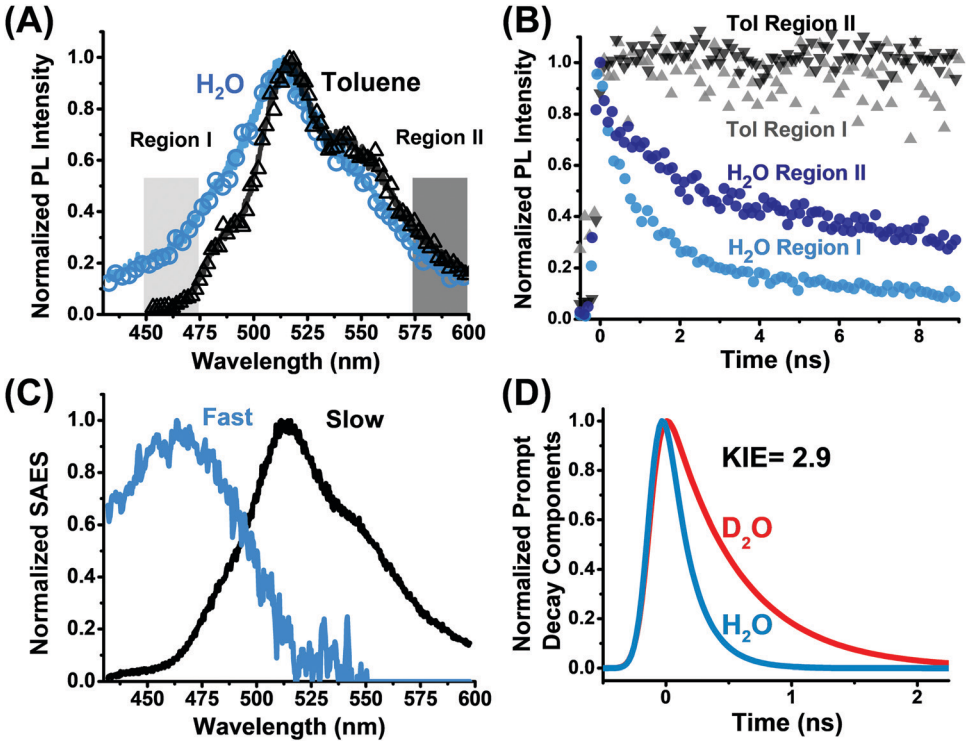

Fig. 5 Time-resolved photoluminescence (TR-PL) of TAHz in water and toluene (365 nm, 100 fs pulse excitation). (A) PL spectra averaged over the first 500 ps after excitation. In water (blue), TAHz exhibit a new PL feature at higher photon energy (region I) compared to TAHz in toluene. Solid lines are globally fitted lines of the data (symbols). (B) PL kinetics traces of TAHz in water (blue) and toluene (black). In toluene, traces from region I and II exhibit identical monoexponential decay kinetics. Decay traces for TAHz in water are distinct from those of region I and II, suggesting two kinetically distinct emissive states exist. (C) Species-associated emission spectra (SAES) from global analysis of the TAHz in water PL exhibit two different spectral components, fast (blue) and slow (black). (D) The prompt decay components of the high-energy emitting species from global analysis for TAHz in D_2O (red) and H_2O (blue). The kinetic isotopic effect (KIE = 2.9), calculated from the lifetime ratio, is consistent with dynamic quenching of the high-energy emission by PCET. Adapted with permission from ref. 113. Copyright 2018 American Chemical Society.

Comprehensive understanding of photochemical reactions in model heptazine systems

I. Measurement and manipulation of molecular properties with substituted phenol substrates

In order to gain further insights regarding the role of hydrogen bonding in the PCET reaction of molecular heptazine photocatalysts, we paired TAHz with para-substituted phenol substrates (R-PhOH) as a model system.[93] As shown in Fig. 6, we observed that the bright ππ* transition in the TAHz absorption spectrum red-shifts upon adding phenol, due to the hydrogen bonding interaction. The fluorescence from the dark ππ* excited state is strongly suppressed due to quenching of excited TAHz by the PCET reaction. The PCET reaction can also be monitored through generation of R-PhO$^{\bullet}$ radical products, probed by EPR spin trapping experiments.[117] Based on first-order association equilibrium analysis of the absorption peak shift[118] and Stern–Volmer analysis of the photoluminescence intensity and lifetime quenching,[119] we were able to quantitatively evaluate some basic properties of the TAHz:R-PhOH photochemistry as follows:

$$\mathrm{TAHz} + \mathrm{R\text{-}PhOH} \rightleftarrows \mathrm{TAHz{:}R\text{-}PhOH}, \quad K_A = \frac{[\mathrm{TAHz{:}R\text{-}PhOH}]}{[\mathrm{TAHz}][\mathrm{R\text{-}PhOH}]} \tag{1}$$

$$\frac{\Delta A_{380\mathrm{nm}}}{l} = \Delta\varepsilon_{380\mathrm{nm}}\left(\frac{[\mathrm{TAHz}]_0 + [\mathrm{R\text{-}PhOH}]_0 + K_A^{-1}}{2}\right) \pm \sqrt{\left(\frac{[\mathrm{TAHz}]_0 + [\mathrm{R\text{-}PhOH}]_0 + K_A^{-1}}{2}\right)^2 - [\mathrm{TAHz}]_0[\mathrm{R\text{-}PhOH}]_0} \tag{2}$$

$$\frac{I_{Fl}^0}{I_{Fl}} = \frac{\tau_{Fl}^0}{\tau_{Fl}} = 1 + k_Q\tau_{Fl}^0[\mathrm{R\text{-}PhOH}]_0 \tag{3}$$

where K_A is the association constant of the ground state complex, $\Delta A_{380\mathrm{nm}}$ is the absorbance change at a given wavelength (in this case, 380 nm), l is the path length of sample cuvette, $\Delta\varepsilon_{380\mathrm{nm}}$ is change of molar extinction coefficient between free TAHz and the TAHz:R-PhOH complex, $[\mathrm{TAHz}]_0$ and $[\mathrm{R\text{-}PhOH}]_0$ are the initial concentrations of each molecule, I_{Fl} and τ_{Fl} are the fluorescence intensity and lifetime of TAHz in phenol–toluene solution, I_{Fl}^0 and τ_{Fl}^0 are the intensity and lifetime of TAHz in pure toluene, and k_Q is the PL quenching constant. We also explored the possibility of multiple hydrogen bonds, due to many nitrogen atoms in the heptazine core, and were able to identify 1 : 1 and 1 : 2 hydrogen-bonded complexes of TAHz and phenol at a higher phenol concentration range

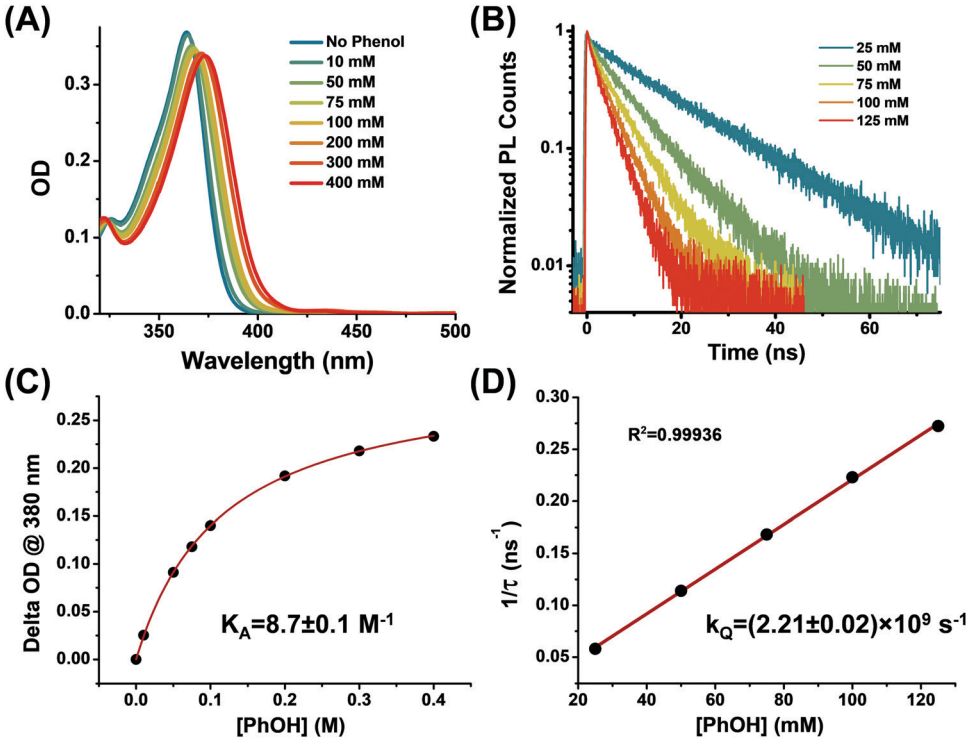

Fig. 6 Evolution of photophysical properties as a function of PhOH concentrations for TAHz solutions in toluene. (A) Absorption spectra. (B) photoluminescence lifetime. (C) Association constant determination from absorption spectral change. (D) Stern–Volmer plot from photoluminescence lifetime change. Reprinted with permission from ref. 93. Copyright 2019 American Chemical Society.

(up to ~900 mM).[120] In following steady-state and time-resolved PL studies, we kept the concentration of R-PhOHs low enough that the dominant hydrogen-bonded species are the 1 : 1 complexes. Parameters obtained from fitting, chemical properties of different R-PhOHs, calculated hydrogen bonding distances and PCET reaction barriers are presented in Table 1.

As shown in Table 1, we were able to manipulate the redox potential of the phenol substrates, and also modulate hydrogen bonding strength between TAHz and R-PhOH, by changing the functional group on the para-substituted phenols.[93] Increasing electron donating strength of the functional group from 4-cyanophenol to 4-methoxyphenol, we observed the following trends in photochemical properties of TAHz:R-PhOH complexes: the association constant (K_A) decreases, while the PCET reaction rate increases, based on the Stern–Volmer quenching rate constant (k_Q). The decrease in K_A, consistent with the calculated hydrogen bonding strength (R_{NH} in Table 1), follows one's chemical intuition that stronger electron donating character of the functional group should result in a less polarized O–H group on the phenol moiety, which ultimately weakens the hydrogen bonding interaction. The increase in the PCET reaction rate that accompanies the larger thermodynamic driving force due to the decreased oxidation potential of R-PhOH also acts to suppress the reaction barrier under the conditions studied here, as described below.

Changing the oxidation potential of R-PhOH has additional implications for the PCET reaction dynamics. Fig. 7 shows the

Table 1 Chemical properties of 4-substituted phenols and their complexes with TAHz in toluene. E_0(R-PhOH$^+$/R-PhOH) is oxidation potential (versus SHE in acetonitrile). pK_a values refer to R-PhOH species in DMSO solvent. k_Q TCSPC or k_Q PLQY are Stern–Volmer quenching constants calculated from photoluminescence lifetime or quantum yield measurements, respectively. K_A is an association constant from absorption measurement. S_1 kinetic isotope effect (KIE) values were calculated from the lifetime of TAHz PL with R-PhOH *vs.* R-PhOD. R_{NH} and $\Delta E^{\ddagger}$ are the hydrogen bonding distance and reaction barrier energy, respectively, from *ab initio* calculations of Hz and R-PhOH complexes. Reprinted with permission from ref. 93. Copyright 2019 American Chemical Society

R	E_0 (R-PhOH$^+$/R-PhOH)[a]	pK_a R-PhOH[b]	k_Q ($\times 10^9$ s^{-1}) TCSPC	k_Q ($\times 10^9$ s^{-1}) PLQY	K_A (M^{-1})	S_1 KIE	R_{NH} (Å)	$\Delta E^{\ddagger}$ (eV)
CN	2.03	13.2	0.556 ± 0.05	0.53 ± 0.02	58 ± 3	1.9 ± 0.1	1.904	0.369
Cl	1.88	16.75	2.78 ± 0.03	2.785 ± 0.007	17.2 ± 0.3	1.36 ± 0.04	1.924	0.169
Br	1.86	16.36	2.73 ± 0.03	3.053 ± 0.009	19.1 ± 0.7	1.36 ± 0.05	1.923	0.177
H	1.88	18.0	2.21 ± 0.02	2.579 ± 0.004	8.7 ± 0.1	1.5 ± 0.1	1.937	0.167
CH_3	1.79	18.9	4.21 ± 0.02	5.124 ± 0.007	8.9 ± 0.2	1.19 ± 0.04	1.940	0.093
OCH_3	1.68	19.1	4.26 ± 0.03	5.218 ± 0.008	8.9 ± 0.4	1.06 ± 0.02	1.943	

[a] Versus SHE in acetonitrile.[121,122] [b] In DMSO.[123]

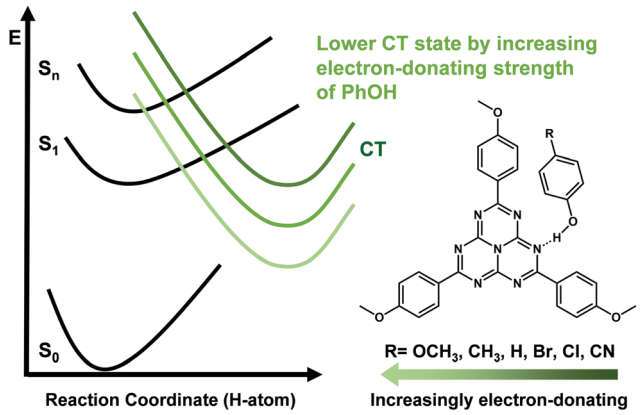

Fig. 7 Schematic depiction of the proposed excited state landscape along the H-atom transfer coordinate from R-PhOH to TAHz. As proposed previously for the TAHz:H_2O complex, there exists a CT state in which an electron moves from the oxygen atom of PhOH to the heptazine core and can drive proton motion. Previous studies with TAHz:H_2O complex suggested the CT state is accessible from higher-lying bright excited states. We hypothesized that the energy curve of the CT state could be stabilized by adding electron-donating groups on the H-atom donor. In this study, we do this by using the series of R-PhOH derivatives depicted above. Reprinted with permission from ref. 93. Copyright 2019 American Chemical Society.

potential energy surface of TAHz:R-PhOH complex along the H atom transfer coordinate. Since molecular orbitals associated with dark $\pi\pi^*(S_1)$ and bright $\pi\pi^*(S_n)$ excited states are localized on the Hz core and anisole moieties of TAHz, one might expect that the energetics of those locally excited states would be minimally affected by changing the R-group on R-PhOH. However, the CT state will be significantly affected upon changes in the oxidation potential of R-PhOH as in Fig. 7. This change in the excited state energy landscape not only tunes the thermodynamic driving force for the PCET reaction, but also the reaction barrier from the local excited state to the charge-transfer state, $\Delta E^{\ddagger}$.

Excited-state reaction barriers were quantitatively evaluated computationally based on relaxed two-dimensional potential energy surfaces, calculated at the lowest energy singlet excited state of the Hz:R-PhOH complex along the H atom transfer coordinate and intermolecular distance between Hz and R-PhOH, as shown in Fig. 8.[93] Consistent with the schematic diagram in Fig. 7, the Hz:R-PhOH complex at the S_1 state must traverse from the Franck–Condon geometry to the biradical product geometry through a saddle point, which is energetically higher than the Franck–Condon geometry by the reaction barrier height, $\Delta E^{\ddagger}$. Calculated $\Delta E^{\ddagger}$ values for different R-PhOH species are shown in Table 1. As expected, $\Delta E^{\ddagger}$ becomes lower as the R-group becomes more electron donating; eventually, at the 4-methoxyphenol limit,

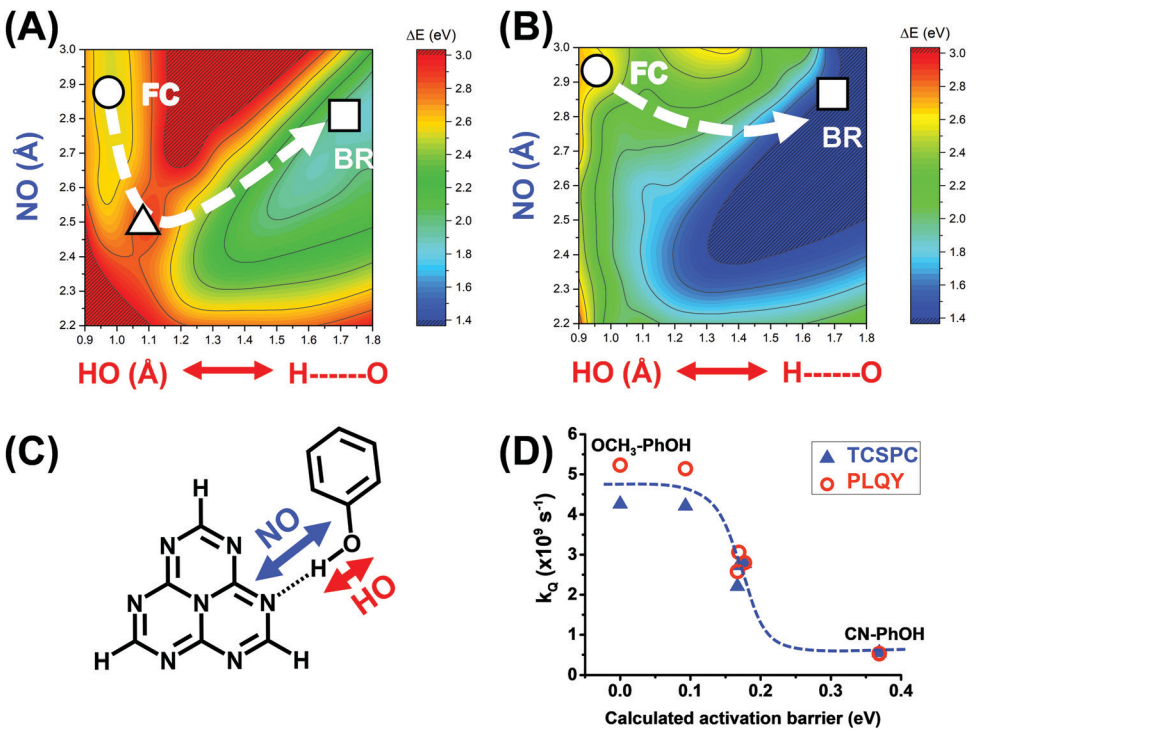

Fig. 8 2D relaxed potential energy surface of the S_1 excited state of the (A) Hz:PhOH complex and (B) Hz:MeOPhOH complex computed at the ADC(2) (second-order algebraic diagrammatic construction) level. The reaction coordinates are the OH bond length of PhOH and the distance between the O-atom of PhOH and N-atom of Hz, see (C). The circle designates the energy minimum of the LE state in the FC region. The square indicates the equilibrium geometry of the HzH$^{\bullet}\cdots$PhO$^{\bullet}$ biradical (BR) formed by H-atom transfer. A saddle point (marked by the triangle) separates the two energy minima. (D) Correlation between the calculated activation barrier and the excited state quenching rate constants, determined by photoluminescence quantum yield (PLQY; red open circles) and lifetime (TCSPC; blue triangles). Overall, we see a significant increase in the excited-state quenching rate as the phenol substituent becomes more electron-donating, becoming saturated at MeOPhOH case. Dashed line is a guide for the eye. Adapted with permission from ref. 93. Copyright 2019 American Chemical Society.

the reaction barrier disappears and PCET becomes barrierless (Fig. 8B). Experimentally, we probed this trend in the activation barrier using Stern–Volmer quenching analysis to assess the rate constants (Fig. 8D) and kinetic isotope effects (KIE) on photoluminescence lifetime between R-PhOH *vs.* R-PhOD (Table 1). By changing the R-group from cyano to methyl, $\Delta E^{\ddagger}$ becomes smaller and the PCET reaction becomes more rapid. Thus, k_Q increases and KIE decreases. At the 4-methoxyphenol limit, the reaction barrier is eliminated, k_Q saturates, and KIE nearly vanishes accordingly.

These experimental trends and computational results revealed a distinct handle for manipulating reactivity of Hz photocatalysts: the redox potential difference between catalyst and substrate. In our case, the substrate side of the catalysis system, R-PhOH, was modified. However, one could envision reversing this approach by changing the redox potential of the Hz catalysts by modifying the pendant groups attached to the Hz core to be stronger electron withdrawing moieties. Another interesting result is the possibility of fine-tuning the reactivity based upon the hydrogen bonding environment. If we compare the 4-chlorophenol to the phenol case in Table 1, the hydrogen bond formation is stronger and the PCET reaction is faster for 4-chlorophenol, while the oxidation potentials for both cases are almost identical. Since the photocatalytic reaction of the TAHz:R-PhOH complex is a combination of electron and proton transfer processes, we suspected that hydrogen bonding interactions also play a considerable role in addition to the primary role that the electrochemical redox potential appears to play. To this end, in the next section, we explore the influence that hydrogen bonding appears to exert on the excited state properties of these intermolecular complexes.

II. The Influence of Hydrogen Bonding on Hz Excited State Geometry

Similarly to the time-resolved emission study of TAHz:H_2O that we described above (Fig. 5), using global target analysis of TR-PL data for TAHz:R-PhOH solutions, we were able to extract wavelength-dependent spectra and time-dependent concentration profiles from distinct emitting species. Data for the specific case of TAHz:PhOH solutions are presented in Fig. 9. In this case, we observe two different emitting species, one with high-energy SAES and sub-nanosecond decay and the other with low-energy SAES and decay kinetics on the order of a few nanoseconds. These components are labelled "fast" and "slow," respectively, in Fig. 9B.[93] Interestingly, when the concentration of PhOH was increased from 25 to 100 mM, only the slow component decay was accelerated and the relative intensity of the fast component SAES increased, while the overall spectral shape of both components remained virtually unchanged. This observation strongly supports the assignment of the low-energy emitting, slow component as free TAHz and the high-energy, fast component as the hydrogen bonded TAHz:PhOH complex. When we applied global analysis to other TAHz:R-PhOH samples, we resolved similar two-component emission behavior as well, except for the 4-methoxyphenol case, wherein, the high-energy emission component is absent on the timescale of our measurement. We interpret this result in terms of barrierless reactivity of the excited TAHz:MeO–PhOH complex, which appears to engage in the PCET reaction prior to emitting measurable fluorescence within the few-picosecond resolution of our streak camera.

Examining the SAES for the hydrogen bonded TAHz:R-PhOH complexes in our TR-PL data allows us to consider their molecular environments and excited state dynamics in further detail. Fig. 10 shows the fast- and slow-component SAES for various R-PhOH species, ranging from 4-cyanophenol to 4-methylphenol.[120] Consistent with the assignment of the fast component being associated with the hydrogen bonded complex and the slow component with free TAHz, the SAES line shape of the fast component exhibits significant variation depending on the R-group of the phenolic species. Conversely, the slow SAES components we observe upon introducing TAHz to the range of R-PhOH derivatives are virtually indistinguishable from the free TAHz emission spectrum in toluene. Intriguingly, the variations in spectral shape of the SAES for the H-bonded species appear to exhibit a clear correlation with the electron donating strength of the R group on the phenol. In particular, while the SAES features all appear to exhibit the same vibronic

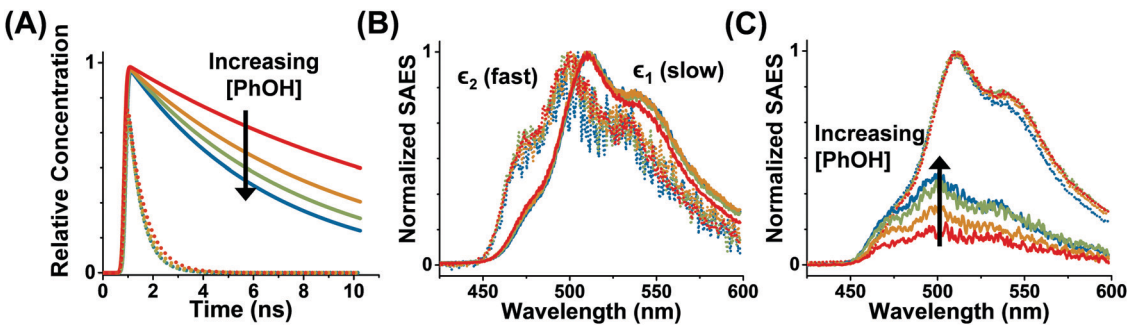

Fig. 9 Global analysis of phenol (PhOH) concentration-dependent TR-PL suggesting that the high energy emitting species is associated with the H-bonded complex, TAHz:PhOH. [PhOH] = 25 mM (red), 50 mM (orange), 75 mM (green), and 100 mM (blue). (A) Kinetic decay rates of slow (solid) and fast (dotted) component with different PhOH concentrations. Slow component decays faster with increasing [PhOH], due to increased Stern–Volmer collisional quenching of unbound TAHz. (B) Normalized SAES reveal that the spectral shape does not appreciably depend on phenol concentration. (C) Intensity of high-energy emission grows with increasing [PhOH] relative to low-energy emission, due to increased H-bonded [TAHz:PhOH] concentration relative to unbound TAHz. Reprinted with permission from ref. 93. Copyright 2019 American Chemical Society.

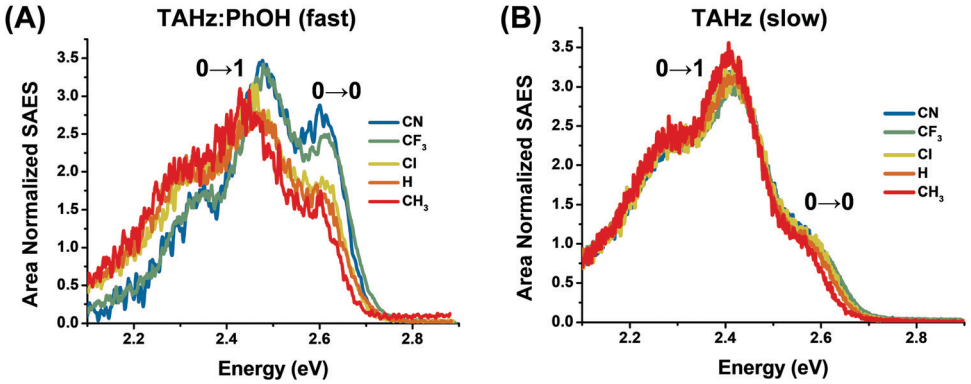

Fig. 10 Species-associated emission spectra (SAES) from global analysis of TR-PL from TAHz with R-PhOH solution. (A) Significant change in the spectral shape of the fast component depending on the R-group of the phenol: CN (blue), CF_3 (green), Cl (yellow), H (orange), CH_3 (red). (B) Slow component spectra show minimal differences among the different R-PhOH. Reprinted with permission from ref. 120. Copyright 2020 American Chemical Society.

peak spacing, the intensity ratios of the different vibronic peaks, the so-called Franck–Condon progression, change quite dramatically.[120] We observe that the highest energy 0–0 vibronic peak becomes more pronounced than the second highest energy or 0–1 peak (Fig. 10A). This variation of spectral shape is not attributable to variations in the solvent dielectric constant, as we observe virtually indistinguishable emission spectra for TAHz in toluene *vs.* a 50 : 50 mixture of toluene and benzonitrile. Referring to the hydrogen bonding association constants in Table 1, we hypothesized that this dramatic distortion of the peak amplitudes, despite no significant variation in the peak spacing, arises as a result of vibronic coupling within the TAHz:R-PhOH complex that influences the extent of the excited state molecular distortion of the TAHz chromophore. As we will describe below, we applied a displaced harmonic oscillator model to capture this trend within the Franck–Condon approximation. We found that stronger hydrogen bonding appears to suppress the nuclear displacement between ground and emitting excited electronic states of TAHz.[120]

Attempts to quantitatively analyze the vibronic structures of TAHz:R-PhOH emission spectra with a single vibrational mode model returned unsatisfactory results. The fast-component SAES cannot be adequately modeled using a single vibrational harmonic oscillator. As in Fig. 11, at least two vibrational oscillators, a high frequency mode at around 1050 cm^{-1} and a low frequency mode at around 200 cm^{-1}, were required to fit all fast-component SAES from the TAHz:R-PhOH complexes with physically reasonable parameters. We implemented a displaced harmonic oscillator model[124,125] where it is assumed that the potential energy surfaces of the electronic ground and excited states comprise the same harmonic potential and where the equilibrium position of the excited state PES is displaced by d_i along a relevant normal mode coordinate Q_i. The displacement can be quantitatively examined by a dimensionless parameter called the Huang–Rhys parameter,[126] $HR_i = d_i^2 m_i \omega_i / 2\hbar$, where m_i is the oscillator effective mass, ω_i is the vibrational frequency of the ith mode, and $\hbar$ is the reduced Planck's constant. Fitting parameters are shown in Fig. 11C and Table 2, along with the electron withdrawing strength of the R-group in the R-PhOH derivatives represented by the Hammett parameter.[127] As we hypothesized from the spectral shape of the fast component SAES, the HR parameter exhibited a clear trend for both vibrational modes, showing less displacement in the excited state with increasing electron withdrawing character of the R-group. A similar effect showing intra- or inter-molecular hydrogen bonding limiting excited state geometric distortion has been studied in other molecular systems using quantum computational methods.[128,129]

It is worth noting a few subtleties related to applying the displaced harmonic oscillator analysis to describe the photophysics of the TAHz chromophore. While our analysis is based on the Franck–Condon and harmonic oscillator approximations, the lowest energy excited state of Hz and TAHz is a dark $\pi\pi^*$ state, which is technically a symmetry-forbidden electric dipole transition. This is noteworthy since there are several cases of highly symmetric chromophores with symmetry-forbidden excited state transitions, such as pyrene, wherein it has been documented that the radiative transition to the ground state cannot be described using only a Franck–Condon type transition, and Herzberg–Teller type transitions[130] or intensity borrowing effects from higher, bright excited states through solvent dipole – chromophore induced dipole interactions[131] must be included to satisfactorily describe the emission spectrum. However, based on density functional theory (DFT) calculations, we observe that the hydrogen bonding interaction from R-PhOH to the pyridinic nitrogens of the Hz core breaks the TAHz molecular symmetry, resulting in a significant increase in the oscillator strength of the otherwise dark low-energy $\pi\pi^*$ transition within the electric dipole Franck–Condon approximation.[120] The oscillator strength induced by this symmetry-breaking effect increases as the R-group of the R-PhOH species becomes more electron withdrawing and the hydrogen bonding interaction in TAHz:R-PhOH becomes stronger. In contrast to the pyrene case, our attempts to model the emission spectra of the TAHz:R-PhOH complexes according to Herzberg–Teller theory could not satisfactorily reproduce the emission line shape when compared with the fits obtained from our displaced oscillator model.

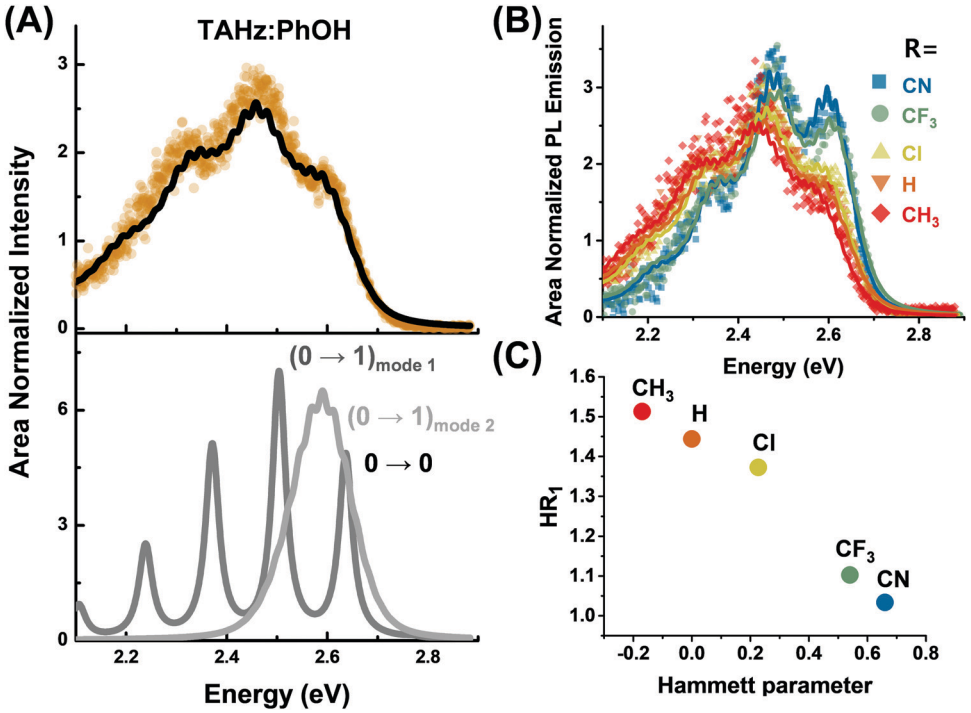

Fig. 11 Fitting of fast component emission spectra with displaced harmonic oscillator model of two vibrational modes. (A) The extracted TAHz:PhOH emission (orange dots) and fitting with the model (black line), assuming two vibrational modes are coupled to the electronic transition: one high frequency mode around 1050 cm^{-1}, one low frequency mode around 200 cm^{-1}. The bottom plot shows the emission spectra from each of the two vibrational modes independently, with the low frequency mode in light grey and the high frequency mode in dark grey. (B) Data (dots) compared to displaced-oscillator model fit (solid lines) for all phenol derivatives. (C) The Huang–Rhys parameter for the high frequency mode as a function of Hammett parameter of the para-substituent on phenol. Greater molecular distortion appears to correlate with weaker hydrogen-bonds (lower Hammett parameters). These data suggest that as the intermolecular hydrogen-bonding interaction becomes stronger, the TAHz chromophore in the complex experiences less excited state geometric distortion. Reprinted with permission from ref. 120. Copyright 2020 American Chemical Society.

To better visualize the types of vibrational motions associated with the intermolecular vibronic coupling that is evident in the fast component emission spectra we observe in Fig. 10, we conducted normal mode analyses using DFT calculations. In Fig. 12A we compare the experimental FT-IR spectrum of TAHz powder with the calculated vibrational spectrum and find that the calculated spectrum agrees adequately with the experimental data. We next compared vibrational frequencies we obtained from our displaced harmonic oscillator fits (Table 2) with the calculated normal modes obtained from DFT for a particular TAHz:R-PhOH complex. Corresponding to the low-frequency mode ($\sim$200 cm^{-1}) in the fitting analysis, we found several Hz ring-puckering modes in our calculated spectra in the range 150–250 cm^{-1}. Therein, the central nitrogen atom in the Hz core is pushed up out of the fused ring plane. This ring-puckering motion is consistent with the optimized geometry of TAHz in the lowest energy dark $\pi\pi^*$ excited state, where the planar symmetry of the Hz ring is broken and the central nitrogen atom pops up in an umbrella-like motion. Since there exist several normal modes with similar ring-puckering motions in our DFT calculations, we conclude that the low-frequency mode and its HR parameter obtained from the displaced oscillator fitting analysis reflect a weighted average of contributing ring-puckering modes.[132]

In the range 1000–1200 cm^{-1}, TAHz exhibits a number of normal modes that are generally attributable to Hz ring-breathing motions. One representative ring-breathing mode of

Table 2 Extracted parameters from fitting with displaced harmonic oscillator model for each vibrational mode. Reprinted with permission from ref. 120. Copyright 2020 American Chemical Society

R	Hammett parameter (σ_p)	Mode 1		Mode 2		Calculated H-bond length (Å)
		Frequency (cm^{-1})	HR_1[a]	Frequency (cm^{-1})	HR_2	
CH_3	−0.17	1068.92 ± 0.04	1.513	128.043 ± 0.004	3.6 ± 0.9	1.940
H	0	1070.37 ± 0.05	1.444	185.68 ± 0.02	2.24 ± 0.02	1.937
Cl	0.227	1061.96 ± 0.04	1.372	159.12 ± 0.01	2.36 ± 0.02	1.924
CF_3	0.54	1057.08 ± 0.05	1.103	179.92 ± 0.04	1.77 ± 0.02	1.910
CN	0.66	1035.49 ± 0.02	1.034	156.800 ± 0.004	1.924 ± 0.007	1.904

[a] Uncertainty $< \pm 10^{-3}$.

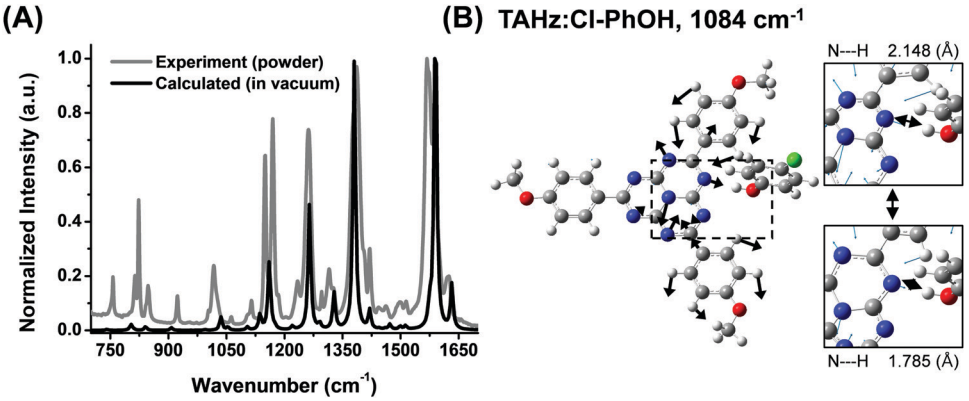

Fig. 12 Vibrational mode analysis. (A) FTIR spectrum of TAHz powder (grey) compared to the calculated FTIR spectrum in vacuum (black, frequency is scaled by 0.97). The vibrational modes in the 1000–1200 cm^{-1} region are generally attributable to heptazine ring breathing and C–N stretching modes. (B) An example heptazine ring-breathing vibration of TAHz:Cl–PhOH complex (1084 cm^{-1}) is shown by the displacement vectors. The high frequency mode extracted from the PL spectral fit is attributable to such modes which are able to break symmetry of Hz ring and modulate hydrogen bonding with PhOH. Reprinted with permission from ref. 120. Copyright 2020 American Chemical Society.

the TAHz:Cl–PhOH complex is shown in Fig. 12B. One relevant feature of the ring-breathing mode is the symmetry breaking effect that it has on the Hz fused ring. Our analysis would suggest that such a displacement of the central and peripheral nitrogen atoms due to this ring-breathing motion may be coupled to the symmetry-breaking effect that supports dipole-allowed emission from the formally dark ππ* transition. With this vibronic character of ring-breathing motion we assigned ring-breathing modes as the high-frequency mode from fitting analysis in Table 2. Another interesting aspect of the ring-breathing motion is that this motion appears to exert a significant modulation of the N–H hydrogen bonding distance. This effect is illustrated in the inset of Fig. 12B. Evidently, the ring-breathing vibrations affects hydrogen bonding between TAHz and R-PhOH and *vice versa*. Thus, stronger hydrogen bonding with R-PhOH can hinder geometry distortion in the ring-breathing normal mode coordinate, which ultimately will be reflected in changes of the vibronic structure in the emission spectrum (Fig. 10). In light of this argument, it is interesting to revisit the different reactivity of 4-chlorophenol *vs.* phenol in Table 1.[93] While both cases have nearly identical driving force for electron transfer, the PCET reactivity appears to be more facile for the 4-chlorophenol, which exhibits stronger hydrogen bonding. From these results, it appears plausible that the PCET reaction is hampered by the geometric distortion of the TAHz excited state, with 4-chlorophenol suppressing this distortion more than phenol, and, hence, showing greater PCET reactivity.

Up to this point, we have considered the effects of chemical modification of the substrate on PCET reactivity. However, considering the nature of the potential energy surfaces along the H atom transfer coordinate, specifically, intermolecular orbital mixing between the chromophore and the substrate may also play a role in facilitating the PCET reaction, as suggested by prior computational results for pyridine,[133] triazine,[134] acridine,[135] and indeed, more recently, for heptazine.[85,88] In particular, for all of these cases mentioned, the hydrogen bonding interactions are not completely innocent, in fact, they play a significant role. That is, the orbitals of the hydrogen bonded complexes comprise hybridized orbital sets with contributions from both the non-bonding orbitals on the heterocycle and p-orbital contributions from the oxygen on the hydroxylic species. In the next section we explore this prospect and demonstrate the ability to manipulate the photochemical reactivity of these complexes using multi-pulse excitations that allow us to access these intermolecular excitations, which appear to be an excited state gateway facilitating the proton-coupled, one-electron oxidation of hydroxyl substrates.

III. In-depth understanding of potential energy surface and laser control of PCET reaction

A schematic diagram of the TAHz:R-PhOH potential energy surface is presented in Fig. 13A. As discussed above, complexation with various R-PhOH species introduces a new reaction path through an intermolecular CT state for TAHz. Hence in the TAHz:R-PhOH complex, some portion of the initial excited state population traverses the CT state surface, while the remainder of the population relaxes into the dark, long-lived ππ* excited state. The relative energy of the CT state, and thus branching ratios among these decay processes, can largely be manipulated by varying the oxidation potential of R-PhOH, as we showed in our previous Stern–Volmer quenching experiments[93] and *ab initio* computation results (Fig. 13B).

Considering the relative energy from the dark ππ* state to the higher-lying TAHz excited states and the intermolecular CT state, we hypothesized that a secondary excitation pulse could be introduced to manipulate the photochemical reactivity of the complex. In this case, the second pulse would re-excite some portion of the TAHz population in the dark ππ* reservoir state, imparting sufficient additional energy to couple to the CT state, allowing the PCET reaction to proceed more efficiently. The dynamics of the re-excited population could then be probed using a third, broadband probe pulse, in a manner similar to conventional pump–probe transient absorption spectroscopy. Similar multi-pulse approaches, or pump–push–probe spectroscopy, have been utilized by a number of research groups to,

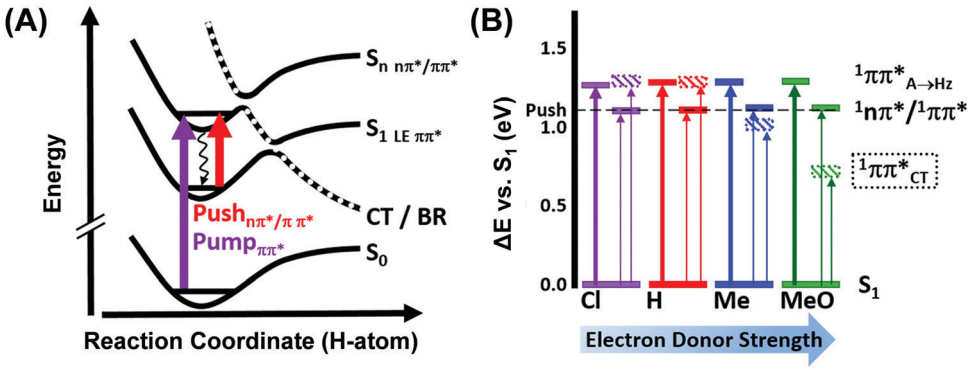

Fig. 13 Schematics of multipulse spectroscopy of TAHz:R-PhOH complexes. (A) Potential energy diagram showing a photochemical proton-transfer reaction driven by an electronic charge-transfer (CT) state, which is strongly stabilized by the proton transfer, resulting in the formation of biradical (BR) products. After initial excitation into a bright S_n state, part of the excited population undergoes rapid radiationless decay (black wavy line) into a long-lived S_1 state. The push pulse can then excite this S_1 state population again into a manifold of mixed $n\pi^*/\pi\pi^*$ states that can efficiently couple to the CT state. (B) Simplified energy diagram depicting vertical electronic transition energies from the relaxed geometry of the S_1 state to the $n\pi^*/\pi\pi^*$ states and intermolecular CT state. While the energies of the locally excited states are independent of the substituent R on phenol, the energy of the CT state is substantially lowered by electron-donating substituents such as Me or MeO. Calculated oscillator strengths for transitions are qualitatively represented by the line widths of the vertical arrows. Reprinted with permission from ref. 117. Copyright 2020 American Chemical Society.

for example, glean in-depth understanding of the photoexcitation dynamics and photocurrent generation in semiconducting materials.[136–138] We employed pump–push–probe spectroscopy for the TAHz:R-PhOH system in order to evaluate the role that higher excited states play in coupling to the reactive CT state pathway and explore the possibility of optically controlling the trajectory of the PCET reaction.[117]

To monitor excited state absorption spectra of free TAHz and the TAHz:R-PhOH complex in the long-lived dark $\pi\pi^*$ state, we initially performed pump–probe TA spectroscopy with TAHz and TAHz:PhOH mixed samples. Fig. 14A shows TA spectra of TAHz only and TAHz with PhOH in toluene. The spectra are time-averaged over pump–probe delay times from 2 to 3 ps. After initial excitation into the bright $\pi\pi^*$ state, TAHz undergoes rapid internal conversion to the dark $\pi\pi^*$ S_1 state on a sub-picosecond timescale. The excited TAHz remains in the long-lived S_1 state for several hundred nanoseconds. This is reflected in the experimental TA spectra, showing that after 2 ps the intensity gradually decays and the spectral shape does not change. This assignment is also corroborated by the fact that the decay kinetics of the NIR TA signal (Fig. 14B) are identical to the time-resolved fluorescence decay of the TAHz S_1 state (not shown here).[117] Based on *ab initio* calculations of the S_1 state (Fig. 13B), we were able to match the spectral features in the excited state absorption spectra with transitions from the dark $\pi\pi^*$ state. The signal in the NIR region corresponds to the near-degenerate bright $\pi\pi^*$ state and another TAHz excited state with $n\pi^*$ character. There also exists a higher energy $\pi\pi^*$ state transition around 1.8 eV from S_1 which matches with the TA signal around ~690 nm. Consistent with observations from TR-PL experiments, adding PhOH quenches the S_1 state population *via* the additional decay and PCET reaction path in the TAHz:PhOH complex and through collisional quenching in the case of free TAHz in the solution. This quenching appears to decrease the signal amplitude (Fig. 14A) and accelerate the decay kinetics (Fig. 14B).

Similarly to TR-PL analysis of TAHz:R-PhOH complexes, we can apply global analysis to the TA data for our TAHz:PhOH samples to recover detailed kinetic information. The data can be modeled with two excited species, one with a fast, ~75 ps decay constant, and the other with a slow, 620 ps decay constant. We attributed the fast component to the TAHz:PhOH complex and the slow component to free TAHz, following our previous analysis of the TR-PL decay kinetics. We selected a pulse wavelength of 1150 nm for the secondary excitation in the pump–push–probe experiment in order to exclusively 'push' only the TAHz:PhOH complex in the S_1 state to the mixed $n\pi^*/\pi\pi^*$ state. This selection was based upon evolution-associated decay spectra (EADS) of each component in Fig. 14C. The 6 ps delay between pump and push pulse was chosen to ensure that complete internal conversion to the S_1 state occurred after the initial excitation and that the push pulse has a chance to interact with the S_1 population before it completely decays.

Fig. 15A shows visible to NIR region TA spectra from toluene solutions of TAHz and a TAHz:R-PhOH, with and without the 1150 nm push pulse (6 ps delay with respect to the 365 nm pump excitation). There are two notable aspects in the data. First, we identified the same general reactivity trend that we observed in our TR-PL data. The R-PhOH species possessing R-groups with greater electron donating character tend to quench more of the excited state TAHz population. Experimentally, this result manifests as decreased signal amplitude in TA spectra among these samples at equivalent pump–probe delays. Interestingly, the spectral shape of the TA signal was completely different, with a peak around 520 nm, in the case of 4-methoxyphenol, where the PCET reaction becomes barrierless. The latter being consistent with TR-PL measurements and quantum chemical calculations. We hypothesized that the excited TAHz:MeO–PhOH complex primarily couples to the CT state and results in biradical products. This may be the origin of the distinct TA spectrum in the MeO–PhOH case, perhaps comprising the TAHz-H$^\bullet$

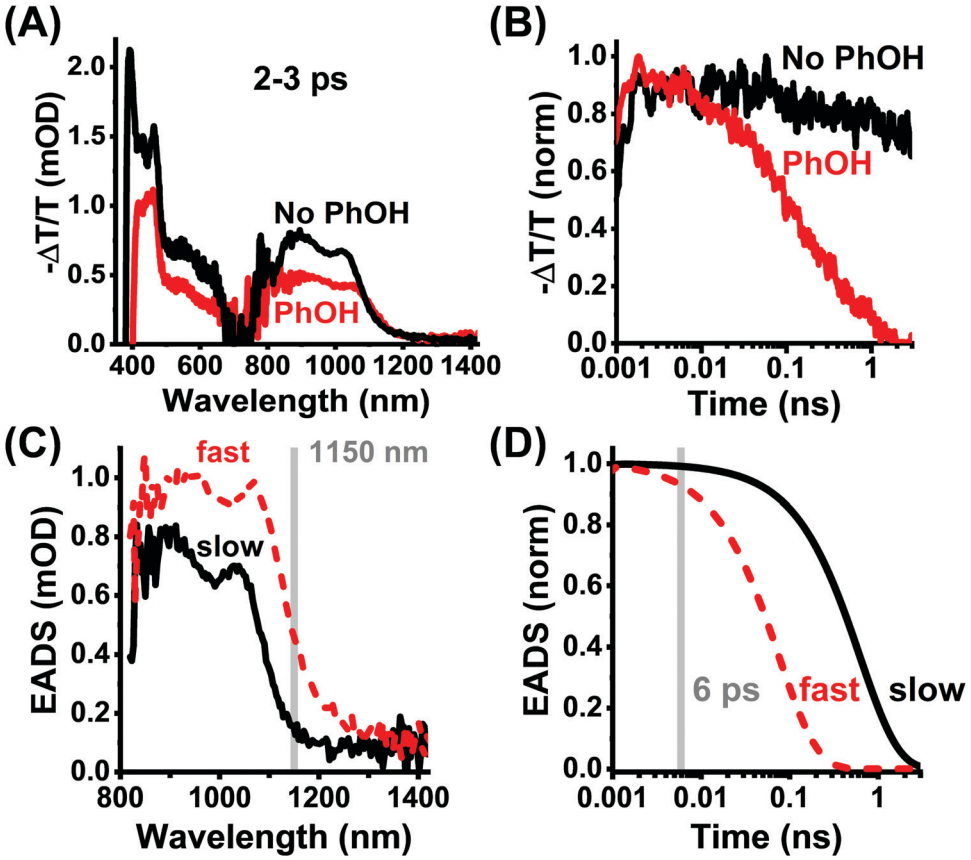

Fig. 14 Excited state absorption spectra of the TAHz:PhOH system measured by transient absorption (TA). (A) TA spectra from the ultraviolet to near-infrared (averaged from 2–3 ps) and (B) decay traces of TAHz (15 μM) with and without PhOH (1.0 M) averaged over 900–1000 nm. (C) Spectra and (D) kinetics from global analysis of the NIR transient absorption feature of TAHz in the presence of PhOH. From the evolution-associated difference spectra (EADS), the push pulse was chosen to be 1150 nm to excite the red edge of the lowest-energy transition for the hydrogen-bonded complex (75 ps decay constant, shown in red). The slow component (shown in black) has a decay constant of 620 ps. Reprinted with permission from ref. 117. Copyright 2020 American Chemical Society.

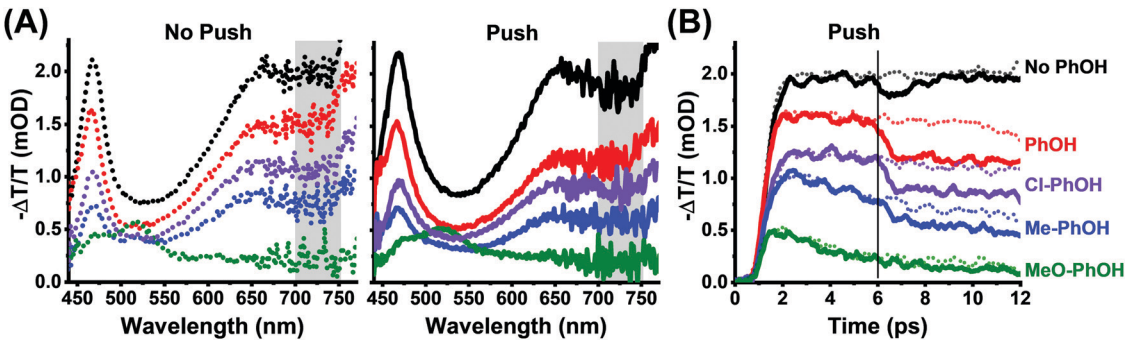

Fig. 15 Effect of push pulse from pump–push–probe spectroscopy. (A) (Left, dotted) Pump–probe spectra of TAHz (50 μM) in toluene with and without phenol derivatives, R-PhOH (1 M). (Right, solid) Pump–push–probe spectra of TAHz (50 μM) in toluene with and without phenol derivatives, R-PhOH (1 M). Spectra were averaged from 6.5–8.0 ps. (B) Decay of the S_1 state population probed from 700–750 nm, shaded in gray in (A), with (solid) and without (dotted) the push pulse. The system was pumped at 365 nm and pushed at 1150 nm at 6 ps. The sample was continuously stirring during the experiment. Reprinted with permission from ref. 117. Copyright 2020 American Chemical Society.

radical absorption. Secondly, the effect of the push pulse appears in the TA spectra, with varying degrees depending on the substrate, as a decrease in the S_1 state population that is concomitant with the arrival of the push pulse. The depletion of the S_1 state population is most clearly discernible in time-resolved decay kinetics in Fig. 15B. We observed that the depopulation of the S_1 state absorption for the TAHz:PhOH case persists following the arrival of the push pulse, which means that the depletion of the S_1 state population is irreversible. In other words, the push pulse drives the S_1 population along an alternate chemical trajectory,

likely *via* the CT state pathway along the PCET reaction coordinate, rather than returning to the dark ππ* state. This result is in sharp contrast to the behavior of the S_1 state in response to the arrival of the push pulse in the TAHz only case, where the CT state is absent. In the TAHz-only case, the re-excited population can only relax back to the S_1 state. Thus, there is only a transient depopulation of the S_1 state and the TA signal exhibits a rapid recovery, approaching the response resolution of our pump–push–probe instrumentation for the TAHz only case.

The results from pump–push–probe experiments are congruous with the molecular picture from our TR-PL experiments and computational analysis, as schematically summarized in Fig. 7. Hydrogen bonding with R-PhOH introduces an intermolecular CT state to the TAHz potential energy surface, along which a portion of the photoexcited population in the bright S_n state can traverse to undergo PCET, resulting in biradical products. On the other hand, the portion of the population that rapidly relaxes into the long-lived S_1 state undergoes a molecular distortion, which opens a pathway for these excitations to be re-excited by the push pulse to a mixed nπ*/ππ* state that can effectively couple to the reactive CT pathway. The relative energy of the CT state compared to other TAHz excited states can be modulated by chemically modifying the R-PhOH oxidation potential, and consequently the branching ratio between PCET path and relaxation to S_1 can be manipulated. In the limit of 4-methoxyphenol, a barrierless PCET reaction condition is achievable and the vast majority of the photoexcited population traverses the reactive CT coordinate. The relative effect of the push pulse, the persistent bleaching of S_1 state absorption signal intensity (Fig. 15), appears to mirror this reactivity trend. The less reactive R-PhOH (phenol) species exhibit large activation barriers and less efficient coupling to the CT state. In this case, due to the higher potential energy barrier, more of the photoexcited population relaxes into the S_1 manifold rather than proceeding into the CT state. The push pulse re-excites a greater fraction of the remaining unreacted TAHz S_1 states to the higher-lying mixed nπ*/ππ* state with phenol than other R-PhOHs. Thus, the fractional push pulse effect that we observe is more pronounced with PhOH than for the other R-PhOH complexes. In the case of 4-methoxyphenol, the photoexcited TAHz primarily engages in the PCET reaction, with little remaining population relaxing to the S_1 state that could be re-excited by the push pulse. Consequently, we observe a vanishingly small effect of the push pulse in the MeO–PhOH case.

Future directions for photoactive heptazines

If one considers the water splitting reaction, the most conceptually simple set of half reactions involves a pair of four-electron and four-proton redox processes, as shown below:[17]

$$\text{Oxidation: } 2H_2O \rightarrow O_2 + 4H^+ + 4e^-, \quad (4)$$

$$\text{Reduction: } 4H^+ + 4e^- \rightarrow 2H_2. \quad (5)$$

Energetically, this water splitting process to generate oxygen and hydrogen must be driven with an external energy source, typically provided by electrical input or a combination of photon energy and electrochemical impulse. To support photon-driven water splitting, sensitizers for absorbing incident light and catalysts for facilitating electron transfer have been explored.[13,17] However, it has been widely recognized that multi-electron redox reactions, especially the four-electron oxidation reaction (eqn (4)), are kinetically unwieldy and this limitation hampers efficient water splitting with diffuse solar illumination.[139] Historically, pathways for water oxidation involving intermediates with radical character have been deliberately avoided, due to the perception that they are inherently untamable energy loss processes.[140] However, that notion presupposes such neutral open-shell species to necessarily be H• or •OH free radicals. In fact, the reducing and oxidizing equivalents generated following a photon-driven cleavage of an intermolecular hydrogen bonded complex by PCET can be stabilized by the surrounding complexation environment. As such, one may conceive of pathways alternative to standard proton reduction for hydrogen generation:[84,100]

$$A\cdots H\text{–}OH + B \rightarrow A\text{–}H^{\bullet} + B\text{–}OH^{\bullet}, \quad (6)$$

$$2(A\text{–}H^{\bullet}) \rightarrow 2A + H_2, \quad (7)$$

$$2(B\text{–}OH^{\bullet}) \rightarrow 2B + H_2O_2, \quad (8)$$

In this case, A is the photoactive catalyst that is capable of hydrogen bonding and excited state PCET and B is a co-catalyst for stabilizing •OH radicals, such as noble metals or metal oxides.[100,141,142] This scenario avoids kinetically cumbersome multi-electron redox processes and may be amendable to utilizing low-intensity light sources, including solar irradiation. In this regard, the Hz molecular catalyst may satisfy two important preconditions for acting as a photoactive catalyst for water splitting: (1) Hz can form hydrogen bonded complexes through its peripheral nitrogen atoms and (2) undergo intermolecular PCET reactions that result in biradical products. In the preceding sections of this Feature Article, we have discussed at length the computational and experimental evidence for these two qualities that our previous research has provided.

One important remaining factor that influences the photochemical reactivity of Hz derivatives may, at first glance, appear to be a rather subtle detail associated with their electronic structures. However, upon further examination, this feature results in important and quite unique behavior. Fig. 16A shows the Hz molecular orbitals associated with the dark ππ* S_1 state, calculated at the ADC(2) level of theory. The HOMO is entirely localized on the peripheral nitrogen atoms, while the LUMO is localized on the carbon atoms. Nearly zero overlap exists among the two MOs,[143] despite their localization on the Hz core of the molecule. The near-zero overlap results in an electron exchange energy that is uncharacteristically small for most organic molecules, such that the singlet and triplet excited states would be, to first order, nearly degenerate. However, due to spin-polarization effects,[144,145] the energy ordering of the S_1 and T_1 states actually becomes inverted with respect to what one would normally anticipate from Hund's multiplicity rules. As a result, the T_1 state is higher in energy than the stabilized S_1 state in Hz derivatives.

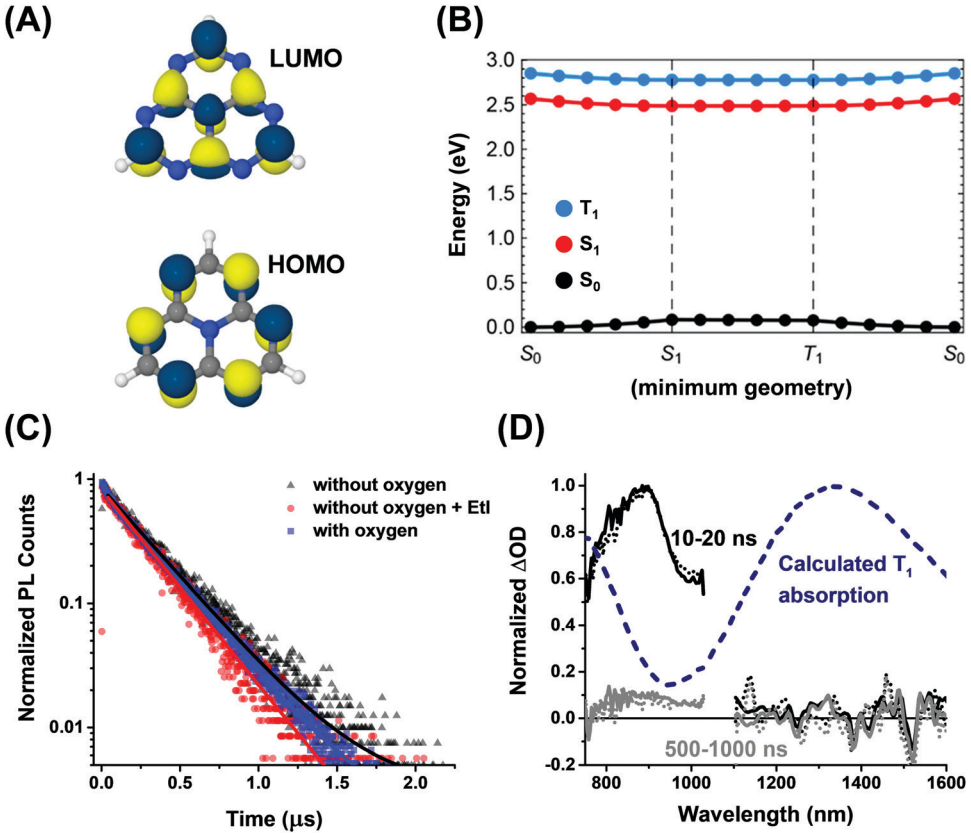

Fig. 16 Relevant molecular orbitals and inverted S_1/T_1 energy of Hz derivatives. (A) Highest occupied (HOMO) and lowest unoccupied (LUMO) Hartree–Fock molecular orbitals of Hz, which constitute the major transition character of the S_1 excited state. (B) Energy profiles of linearly interpolated scans between the S_0 minimum geometry, the S_1 minimum geometry, and the T_1 minimum geometry of Hz, calculated at the ADC(2) level. The energy of the T_1 state (blue) is above the energy of the S_1 state (red) throughout. Black trace corresponds to the energy of the S_0 state at each geometry. (C) Emission lifetimes of TAHz in toluene show very little dependence on the presence of oxygen or a heavy atom source, such as ethyl iodide (EtI). Comparing the emission decay with (blue) and without oxygen (black), and at various temperatures, we see no evidence for a low energy triplet quenching pathway or thermally activated delayed florescence. (D) TA spectra with (dotted) and without (solid) the presence of a heavy atom at early (black) and long (gray) timescales. Data show no significant difference. For comparison, calculated triplet state absorption (dashed line) is also presented. Reprinted with permission from ref. 143. Copyright 2019 American Chemical Society.

Since observing this stabilization computationally requires coupling with double excitations,[144] the correct energy ordering for these states cannot be recovered using DFT methods, whereas it is readily observed in the ADC(2) calculations for several Hz derivatives (Fig. 16B). Moreover, we applied a number of spectroscopic methods to assess the qualitative energy ordering of these different spin states. TR-PL experiments conducted for TAHz under aerobic *vs.* anaerobic conditions, as well as in the presence of an external heavy atom sensitizer (Fig. 16C) all indicated the absence of a viable low-energy triplet pathway by which the S_1 state can be quenched.[143] We obtained analogous results using transient absorption spectroscopy (Fig. 16D). The unique nature of the intersystem crossing to T_1 from S_1 being energetically uphill in Hz derivatives, means that deactivation of the photoexcited S_1 state has only two primary deactivation pathways, photon emission or internal conversion to S_0. We stressed earlier that the dark $\pi\pi^*$ transition in Hz and its derivatives is symmetry-forbidden, however, since the energy gap between the S_1 and the S_0 state is relatively large, the rate constant for internal conversion between these states is small, in accord with Energy Gap Law.[146] Therefore, despite the weak oscillator strength for the S_1 transition, which leads to a particularly long fluorescence lifetime (287 ns), the fluorescence quantum yield is unexpectedly high ($\sim$70% in toluene).[113] This combination of unusual attributes allows the S_1 excitations to act as long-lived reservoir states for photochemical reactions, while avoiding generating long-lived triplet excitations that would be susceptible to sensitizing reactive singlet oxygen that can destroy the catalyst. The latter is a common drawback associated with photocatalysts that rely on generating triplet excited states with lifetimes long enough to outlast the slow timescales for molecular diffusion.

Apart from the PCET reactivity and biradical formation, it is also worth considering the subsequent reactivity of the heptazinyl radical (HzH$^\bullet$) and its potential photochemistry following the initial H atom abstraction.[147] Fig. 17 illustrates a computational survey of the excited states of HzH$^\bullet$. Notably, one of the electronic excited states of the heptazinyl radical exhibits dissociative character along the Hz–H$^\bullet$ bond axis. Excitation of HzH$^\bullet$ into this dissociative $\pi\sigma^*$ state, where the electron occupies a Rydberg-type orbital, will result in H$^\bullet$ radical emission. This process would

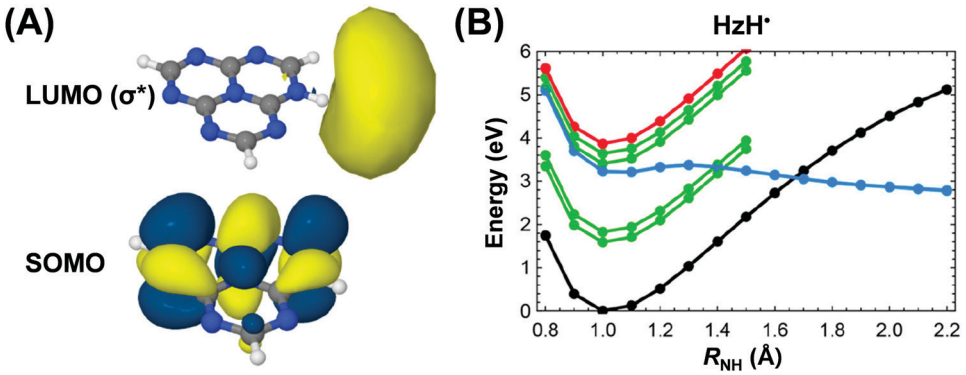

Fig. 17 Heptazinyl radical photodissociation. (A) Singly occupied molecular orbital (SOMO) and the unoccupied diffusive σ* orbital involved in the excitation of the $^2\pi\sigma^*$ state of the HzH• radical. (B) Potential energy surface of HzH• radical along N–H distance. Black = ground state, green = ππ* excited states, red = nπ* excited states, blue = repulsive πσ* state. The repulsive πσ* state provides a photodissociation channel for H atom detachment reaction. Reprinted with permission from ref. 147. Copyright 2020 American Chemical Society.

restore the closed-shell ground state neutral Hz chromophore, which can then ultimately reengage in subsequent PCET reactions with additional substrate molecules. In this scenario, light energy will be converted into reactive H• and substrate radical, which can be used to facilitate subsequent reactions, while the Hz catalyst is regenerated, avoiding persistent chemical decomposition. Based on this result, photocatalysis and catalyst regeneration are viable through a multi-pulse excitation scheme, without degradation from side reactions. The multi-pulse experiments are currently ongoing in order to spectroscopically probe biradical products and also photoexcite the product into the dissociative electronic state, exploring another possibility of manipulation of heptazine photochemistry.

Experimental and computational evidence suggests that one major factor determining PCET reactivity between the TAHz catalyst and the R-PhOH substrate is the nature of the barrier between the non-reactive TAHz electronic states and the reactive intermolecular CT states of the complex.[93] We were able to tune the reactivity in our previous studies by changing the R-group of the R-PhOH substrate, due simply to a change in oxidation potential. Considering the fact that the relative energy is important in determining PCET reactivity, one can envisage that a reciprocal strategy could be employed by incorporating electron withdrawing pendant groups on the Hz core to tune the CT state energy barrier and increase PCET reactivity (Fig. 18).[147] One of the most important substrates in photocatalysis, the water molecule, cannot be modified as R-PhOH, and thus we can modify Hz catalysts itself to optimize reactivity for more efficient water oxidation chemistry. Synthetic approaches in this respect are currently ongoing in our lab. We also continue to explore multi-pulse excitation schemes to better understand photochemistry of heptazine derivatives in greater detail and develop more effective molecular photocatalyst systems.

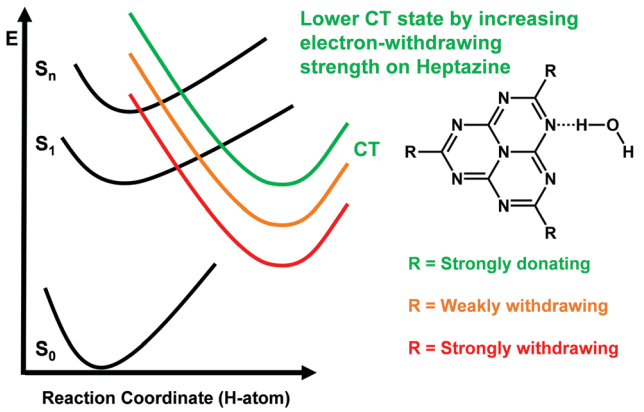

Fig. 18 Schematic diagram of potential energy surfaces for substituted Hz:H_2O complexes, illustrating the relationship between the relative energy of the CT state and the PCET barrier on the PE surface of the S_1 state. Reprinted with permission from ref. 147. Copyright 2020 American Chemical Society.

Summary

In this Feature Article, we presented our recent research efforts regarding the photochemistry of polymeric g-C_3N_4 and derivatives of its structural monomer unit, heptazine (Hz). From our initial time-resolved spectroscopic analysis on g-C_3N_4 and exfoliated C_3N_4[102] we speculated that the primary reactive sites where photocatalysis occurs may be molecular Hz sub-units of g-C_3N_4.[110] Computational analysis of Hz derivatives and other N-heterocyclic molecules suggests that hydrogen bond formation and subsequent PCET reactions may influence g-C_3N_4 photocatalysis, leading to prospects for thermodynamic and kinetic advantages.[88] Consistent with this prediction, we experimentally observed that our model Hz derivative, TAHz, can form hydrogen bonded complexes with water, undergo photon-driven PCET, and generate •OH and H_2 products.[113] Using R-PhOH substrates, we were able to uncover additional quantitative assessments of hydrogen bonding strength and PCET reactivity related to spectroscopically-determined association constants and Stern–Volmer quenching rate constants.[93] The results followed a general trend that the oxidation potential of the R-PhOH species is a primary factor governing the activity, such that a substrate with lower oxidation potential is more likely to transfer its electron to TAHz. That is, couple to the intermolecular CT state and progress along the

PCET reaction pathway. *Ab initio* calculations successfully reproduced the same trend as the experimental results. The barrierless PCET condition is experimentally achievable using the 4-methoxyphenol substrate. Additionally, we were able to analyze aspects of the molecular environment and its influence on the properties of excited-state TAHz:R-PHOH complexes through a vibronic analysis of their time-resolved emission spectra. Fitting the TR-PL data from the hydrogen bonded complex with a multimode displaced harmonic oscillator model and comparing the result with DFT calculation,[120] indicates that increasing the electron withdrawing character of the R-group (higher Hammett parameter) induces stronger hydrogen bonding between TAHz and R-PhOH. This H-bonding effect evidently suppresses the geometric distortion between the S_1 state and the S_0 ground state. Consequently, we observe a lower Huang–Rhys parameter in the measured fluorescence spectra with increasing Hammett parameter. Manipulating the hydrogen bonding strength may provide an additional control knob for tuning PCET reactivity, which is evidently at play in cases of similar redox potentials of the Hz derivative or the substrate, such as in the instance of TAHz:PhOH *vs.* TAHz:Cl-PhOH. Lastly, we explored another possible way to control the TAHz photoreaction: optical control with multi-pulse spectroscopy.[117] When we introduced a NIR secondary excitation pulse (the push pulse in Fig. 13) that can excite TAHz in the S_1 state into higher excited states, we observed a persistent depletion of the S_1 state population of the TAHz:PhOH complex. This is in contrast to the free TAHz case, wherein the depletion is only transient. The amount of depletion also followed the trend in the PCET reactivity of the R-PhOH species, which is consistent with the molecular picture from our previous TR-PL studies. That is, a greater fraction of the initially excited population proceeds along the PCET pathway as the R-PhOH species becomes easier to oxidize. Thus, fewer of the excited complexes relax into the S_1 state to be re-excited by the push pulse. Since the push-induced depletions of the population does relax back to the S_1 state, the implication is that this re-excited population has coupled into the reactive intermolecular CT state as a result of the additional energy imparted by the push pulse.

In this Feature Article, we focus primarily on light-driven water oxidation reactions of Hz-based materials. However, it is also a critical challenge to understand analogous molecular mechanisms involved in other important chemical transformations, such as CO_2 reduction, which has been reviewed extensively in the literature.[148–150] For example, recently, Domcke, Sobolewski and coworkers predicted that pyridinyl radicals are capable of hydrogen-bonding with and chemically reducing CO_2 by photoinduced PCET.[151] The authors noted that a similar mechanism may provide insight into the photocatalytic reduction of CO_2 by g-C_3N_4. The implication being that photogenerated heptazinyl radicals ($HzH^{\bullet}$) can form hydrogen-bonded complexes with CO_2. The complexes can then photodissociate by a PCET process to liberate hydroxyformyl radicals. Recent experimental studies indicate that employing co-polymerization[152] or introducing structural defects[153–155] to C_3N_4 can increase activity toward CO_2 reduction. Our work suggests that experimental approaches utilizing model molecular Hz derivatives may provide additional insight into the CO_2 reduction mechanisms for C_3N_4. Hydroamidation reactions are another notable class of transformations that have recently been affected using C_3N_4-based photocatalysts. In a recent example from Nocera and coworkers, the authors demonstrated that cyanamide-modified C_3N_4 can initiate a light-driven PCET process that catalyzes a hydroamidation photoredox cycle involving a number of H-atom transfer steps.[55]

While this Feature Article has primarily dealt with optical spectroscopic techniques such as time-resolved photoluminescence and transient absorption spectroscopy, other time-resolved methods may provide additional insight into the photoreactivity mechanisms of C_3N_4 and heptazine-based materials. For example, a recent two-dimensional IR analysis revealed the picosecond intramolecular vibrational energy redistribution process in g-C_3N_4.[156] Time-resolved microwave conductivity[157] and optical-pump terahertz-probe spectroscopy[158] have also been used to directly measure photoconductivity of C_3N_4-based catalysts, correlating conductivity with catalytic efficiency.

Finally, the inverted S_1/T_1 energy splittings (ΔE_{ST}) that Hz derivatives exhibit remain one of their truly remarkable attributes. Arising from the combination of higher-order spin polarization effects and their localized, but non-overlapping HOMO and LUMO character, this ΔE_{ST} inversion, paired with the forbidden nature of the S_1 fluorescence, leads to an uncharacteristically high fluorescence quantum efficiency ($\sim$70%) for a material with such a long fluorescence lifetime ($\sim$300 ns).[143] These photophysical properties are important for photochemical applications because they allow the S_1 state to serve as a long-lived energy reservoir, supporting molecular diffusion, while avoiding the sensitization of indiscriminately-reactive singlet oxygen. The latter often induces uncontrollable catalyst degradation and plagues many long-lived triplet photocatalytic systems.

It also seems likely that Hz-based materials will serve as a model testbed for better understanding and applying inverted ΔE_{ST} motifs in the field of thin-film optoelectronic materials and devices that incorporate organic semiconductor components. This will undoubtedly be particularly true for organic LEDs and organic photovoltaics, where device performance is often sensitive to recombination processes involving triplet excitons. The same may perhaps be true even for perovskite-based devices that incorporate organic charge transport layers. All told, Hz-based materials appear poised to be of increasing relevance for numerous potential applications, ranging from photocatalysis for sustainable energy technologies and preparatory photochemistry to solid-state optoelectronic materials and devices.

Author contributions

The manuscript was written through contributions of all authors. All authors have given approval to the final version of the manuscript.

Conflicts of interest

The authors declare that there are no competing financial interests.

Acknowledgements

This work is based on research that was supported in part by the Washington Research Foundation and the University of Washington Clean Energy Institute (CEI). Part of this work was conducted at the Molecular Analysis Facility, a National Nanotechnology Coordinated Infrastructure (NNCI) site at the University of Washington, which is supported in part by funds from the National Science Foundation (awards NNCI-2025489, NNCI-1542101), the Molecular Engineering & Sciences Institute, and the Clean Energy Institute. DFT and TD-DFT calculations were facilitated through the use of advanced computational, storage, and networking infrastructure provided by the Hyak supercomputer system and funded by the STF at the University of Washington. C. W. S. acknowledges that a portion of this material is based upon work supported by the US National Science Foundation (NSF) under Grant No. [1846480]. We would also like to express our appreciation to Prof. Dr habil. Wolfgang Domcke and Prof. Dr hab. Andrzej L. Sobolewski for their invaluable *ab initio* computational contributions to many of the works discussed in this article.

References

1 N. S. Lewis, Research opportunities to advance solar energy utilization, *Science*, 2016, **351**(6271), aad1920.
2 Y. Qu and X. Duan, Progress, challenge and perspective of heterogeneous photocatalysts, *Chem. Soc. Rev.*, 2013, **42**(7), 2568–2580.
3 C. Battaglia, A. Cuevas and S. De Wolf, High-efficiency crystalline silicon solar cells: status and perspectives, *Energy Environ. Sci.*, 2016, **9**(5), 1552–1576.
4 J. Gong, C. Li and M. R. Wasielewski, Advances in solar energy conversion, *Chem. Soc. Rev.*, 2019, **48**(7), 1862–1864.
5 M. H. Shaw, J. Twilton and D. W. MacMillan, Photoredox Catalysis in Organic Chemistry, *J. Org. Chem.*, 2016, **81**(16), 6898–6926.
6 E. C. Gentry and R. R. Knowles, Synthetic Applications of Proton-Coupled Electron Transfer, *Acc. Chem. Res.*, 2016, **49**(8), 1546–1556.
7 A. Savateev and M. Antonietti, Heterogeneous organocatalysis for photoredox chemistry, *ACS Catal.*, 2018, **8**(10), 9790–9808.
8 S. Protti, M. Fagnoni and D. Ravelli, Photocatalytic C–H Activation by Hydrogen-Atom Transfer in Synthesis, *ChemCatChem*, 2015, **7**(10), 1516–1523.
9 J. C. Colmenares and R. Luque, Heterogeneous photocatalytic nanomaterials: prospects and challenges in selective transformations of biomass-derived compounds, *Chem. Soc. Rev.*, 2014, **43**(3), 765–778.
10 J. Rugolo and M. J. Aziz, Electricity storage for intermittent renewable sources, *Energy Environ. Sci.*, 2012, **5**(5), 7151–7160.
11 M. R. Shaner, S. J. Davis, N. S. Lewis and K. Caldeira, Geophysical constraints on the reliability of solar and wind power in the United States, *Energy Environ. Sci.*, 2018, **11**(4), 914–925.
12 B. A. Pinaud, J. D. Benck, L. C. Seitz, A. J. Forman, Z. Chen, T. G. Deutsch, B. D. James, K. N. Baum, G. N. Baum and S. Ardo, Technical and economic feasibility of centralized facilities for solar hydrogen production via photocatalysis and photoelectrochemistry, *Energy Environ. Sci.*, 2013, **6**(7), 1983–2002.
13 K. Maeda and K. Domen, Photocatalytic water splitting: recent progress and future challenges, *J. Phys. Chem. Lett.*, 2010, **1**(18), 2655–2661.
14 K. Takanabe, Photocatalytic water splitting: quantitative approaches toward photocatalyst by design, *ACS Catal.*, 2017, **7**(11), 8006–8022.
15 M. G. Walter, E. L. Warren, J. R. McKone, S. W. Boettcher, Q. Mi, E. A. Santori and N. S. Lewis, Solar water splitting cells, *Chem. Rev.*, 2010, **110**(11), 6446–6473.
16 J. Li, R. Güttinger, R. Moré, F. Song, W. Wan and G. R. Patzke, Frontiers of water oxidation: the quest for true catalysts, *Chem. Soc. Rev.*, 2017, **46**(20), 6124–6147.
17 J. D. Blakemore, R. H. Crabtree and G. W. Brudvig, Molecular Catalysts for Water Oxidation, *Chem. Rev.*, 2015, **115**(23), 12974–13005.
18 M. D. Karkas, Photochemical generation of nitrogen-centered amidyl, hydrazonyl, and imidyl radicals: methodology developments and catalytic applications, *ACS Catal.*, 2017, **7**(8), 4999–5022.
19 U. I. Gaya and A. H. Abdullah, Heterogeneous photocatalytic degradation of organic contaminants over titanium dioxide: a review of fundamentals, progress and problems, *J. Photochem. Photobiol., C*, 2008, **9**(1), 1–12.
20 C.-C. Wang, J.-R. Li, X.-L. Lv, Y.-Q. Zhang and G. Guo, Photocatalytic organic pollutants degradation in metal–organic frameworks, *Energy Environ. Sci.*, 2014, **7**(9), 2831–2867.
21 S. Hammes-Schiffer, Controlling Electrons and Protons through Theory: Molecular Electrocatalysts to Nanoparticles, *Acc. Chem. Res.*, 2018, **51**(9), 1975–1983.
22 C. J. Gagliardi, A. K. Vannucci, J. J. Concepcion, Z. Chen and T. J. Meyer, The role of proton coupled electron transfer in water oxidation, *Energy Environ. Sci.*, 2012, **5**(7), 7704–7717.
23 M. Bourrez, R. Steinmetz, S. Ott, F. Gloaguen and L. Hammarström, Concerted proton-coupled electron transfer from a metal-hydride complex, *Nat. Chem.*, 2014, **7**(2), 140–145.
24 T. Liu, M. Guo, A. Orthaber, R. Lomoth, M. Lundberg, S. Ott and L. Hammarström, Accelerating proton-coupled electron transfer of metal hydrides in catalyst model reactions, *Nat. Chem.*, 2018, **10**(8), 881–887.
25 R. Tyburski, T. Liu, S. D. Glover and L. Hammarström, Proton-Coupled Electron Transfer Guidelines, Fair and Square, *J. Am. Chem. Soc.*, 2021, **143**(2), 560–576.
26 P. V. Kamat and J. A. Christians, Solar Cells versus Solar Fuels: Two Different Outcomes, *J. Phys. Chem. Lett.*, 2015, **6**(10), 1917–1918.
27 S. Chu, W. Li, Y. Yan, T. Hamann, I. Shih, D. Wang and Z. Mi, Roadmap on solar water splitting: current status and future prospects, *Nano Futures*, 2017, **1**(2), 022001.
28 S. Hu, C. Xiang, S. Haussener, A. D. Berger and N. S. Lewis, An analysis of the optimal band gaps of light absorbers in integrated tandem photoelectrochemical water-splitting systems, *Energy Environ. Sci.*, 2013, **6**(10), 2984–2993.
29 J. Jia, L. C. Seitz, J. D. Benck, Y. Huo, Y. Chen, J. W. Ng, T. Bilir, J. S. Harris and T. F. Jaramillo, Solar water splitting by photovoltaic-electrolysis with a solar-to-hydrogen efficiency over 30, *Nat. Commun.*, 2016, **7**, 13237.
30 W.-H. Cheng, M. H. Richter, M. M. May, J. Ohlmann, D. Lackner, F. Dimroth, T. Hannappel, H. A. Atwater and H.-J. Lewerenz, Monolithic photoelectrochemical device for direct water splitting with 19% efficiency, *ACS Energy Lett.*, 2018, **3**(8), 1795–1800.
31 M. R. Shaner, H. A. Atwater, N. S. Lewis and E. W. McFarland, A comparative technoeconomic analysis of renewable hydrogen production using solar energy, *Energy Environ. Sci.*, 2016, **9**(7), 2354–2371.
32 B. D. James, G. N. Baum, J. Perez and K. N. Baum, Technoeconomic analysis of photoelectrochemical (PEC) hydrogen production, *DOE Rep.*, 2009, DOI: 10.2172/1218403.
33 A. Kudo and Y. Miseki, Heterogeneous photocatalyst materials for water splitting, *Chem. Soc. Rev.*, 2009, **38**(1), 253–278.
34 Q. Wang and K. Domen, Particulate Photocatalysts for Light-Driven Water Splitting: Mechanisms, Challenges, and Design Strategies, *Chem. Rev.*, 2020, **120**(2), 919–985.
35 Y. Xu, M. Kraft and R. Xu, Metal-free carbonaceous electrocatalysts and photocatalysts for water splitting, *Chem. Soc. Rev.*, 2016, **45**(11), 3039–3052.
36 M. Z. Rahman, M. G. Kibria and C. B. Mullins, Metal-free photocatalysts for hydrogen evolution, *Chem. Soc. Rev.*, 2020, **49**(6), 1887–1931.
37 L. Li, W.-Y. Lo, Z. Cai, N. Zhang and L. Yu, Donor–acceptor porous conjugated polymers for photocatalytic hydrogen production: the importance of acceptor comonomer, *Macromolecules*, 2016, **49**(18), 6903–6909.
38 H. Y. Chen and S. Ardo, Direct observation of sequential oxidations of a titania-bound molecular proxy catalyst generated through illumination of molecular sensitizers, *Nat. Chem.*, 2018, **10**(1), 17–23.
39 J. L. Bredas and G. B. Street, Polarons, bipolarons, and solitons in conducting polymers, *Acc. Chem. Res.*, 1985, **18**(10), 309–315.
40 J. V. Caspar, V. Ramamurthy and D. R. Corbin, Preparation and spectroscopic characterization of polarons and bipolarons of thiophene oligomers within the channels of pentasil zeolites: the evolution of organic radical ions into conducting polymers, *J. Am. Chem. Soc.*, 1991, **113**(2), 600–610.

41 S. Zheng, S. Barlow, C. Risko, T. L. Kinnibrugh, V. N. Khrustalev, S. C. Jones, M. Y. Antipin, N. M. Tucker, T. V. Timofeeva and V. Coropceanu, Isolation and crystal structures of two singlet bis (triarylamine) dications with nonquinoidal geometries, *J. Am. Chem. Soc.*, 2006, **128**(6), 1812–1817.
42 R. Dhanker, C. L. Gray, S. Mukhopadhyay, S. Nunez, C. Y. Cheng, A. N. Sokolov and N. C. Giebink, Large bipolaron density at organic semiconductor/electrode interfaces, *Nat. Commun.*, 2017, **8**(1), 2252.
43 S. Cao, J. Low, J. Yu and M. Jaroniec, Polymeric photocatalysts based on graphitic carbon nitride, *Adv. Mater.*, 2015, **27**(13), 2150–2176.
44 W. J. Ong, L. L. Tan, Y. H. Ng, S. T. Yong and S. P. Chai, Graphitic Carbon Nitride ($g\text{-}C_3N_4$)-Based Photocatalysts for Artificial Photosynthesis and Environmental Remediation: Are We a Step Closer To Achieving Sustainability?, *Chem. Rev.*, 2016, **116**(12), 7159–7329.
45 Z. Zhou, Y. Zhang, Y. Shen and S. Liu, Molecular engineering of polymeric carbon nitride: advancing applications from photocatalysis to biosensing and more, *Chem. Soc. Rev.*, 2018, **47**(7), 2298–2321.
46 Y. Wang, A. Vogel, M. Sachs, R. S. Sprick, L. Wilbraham, S. J. Moniz, R. Godin, M. A. Zwijnenburg, J. R. Durrant and A. I. Cooper, Current understanding and challenges of solar-driven hydrogen generation using polymeric photocatalysts, *Nat. Energy*, 2019, 1–15.
47 I. Ghosh, J. Khamrai, A. Savateev, N. Shlapakov, M. Antonietti and B. König, Organic semiconductor photocatalyst can bifunctionalize arenes and heteroarenes, *Science*, 2019, **365**(6451), 360–366.
48 G. Zhang, L. Lin, G. Li, Y. Zhang, A. Savateev, S. Zafeiratos, X. Wang and M. Antonietti, Ionothermal Synthesis of Triazine-Heptazine-Based Copolymers with Apparent Quantum Yields of 60% at 420 nm for Solar Hydrogen Production from "Sea Water", *Angew. Chem., Int. Ed.*, 2018, **57**(30), 9372–9376.
49 Q. Han, Z. Cheng, B. Wang, H. Zhang and L. Qu, Significant Enhancement of Visible-Light-Driven Hydrogen Evolution by Structure Regulation of Carbon Nitrides, *ACS Nano*, 2018, **12**(6), 5221–5227.
50 M. J. Bojdys, J. O. Müller, M. Antonietti and A. Thomas, Ionothermal synthesis of crystalline, condensed, graphitic carbon nitride, *Chemistry*, 2008, **14**(27), 8177–8182.
51 X. Wang, K. Maeda, A. Thomas, K. Takanabe, G. Xin, J. M. Carlsson, K. Domen and M. Antonietti, A metal-free polymeric photocatalyst for hydrogen production from water under visible light, *Nat. Mater.*, 2009, **8**(1), 76–80.
52 R. Kuriki, O. Ishitani and K. Maeda, Unique Solvent Effects on Visible-Light CO_2 Reduction over Ruthenium(II)-Complex/Carbon Nitride Hybrid Photocatalysts, *ACS Appl. Mater. Interfaces*, 2016, **8**(9), 6011–6018.
53 Y. Cui, Z. Ding, P. Liu, M. Antonietti, X. Fu and X. Wang, Metal-free activation of H_2O_2 by $g\text{-}C_3N_4$ under visible light irradiation for the degradation of organic pollutants, *Phys. Chem. Chem. Phys.*, 2012, **14**(4), 1455–1462.
54 Y. Qin, B. C. Martindale, R. Sun, A. J. Rieth and D. G. Nocera, Solar-driven tandem photoredox nickel-catalysed cross-coupling using modified carbon nitride, *Chem. Sci.*, 2020, **11**(28), 7456–7461.
55 A. J. Rieth, Y. Qin, B. C. Martindale and D. G. Nocera, Long-Lived Triplet Excited State in a Heterogeneous Modified Carbon Nitride Photocatalyst, *J. Am. Chem. Soc.*, 2021, **143**(12), 4646–4652.
56 J. Xu, L. Zhang, R. Shi and Y. Zhu, Chemical exfoliation of graphitic carbon nitride for efficient heterogeneous photocatalysis, *J. Mater. Chem. A*, 2013, **1**(46), 14766–14772.
57 V. W. H. Lau, V. W. Z. Yu, F. Ehrat, T. Botari, I. Moudrakovski, T. Simon, V. Duppel, E. Medina, J. K. Stolarczyk, J. Feldmann, V. Blum and B. V. Lotsch, Urea-Modified Carbon Nitrides: Enhancing Photocatalytic Hydrogen Evolution by Rational Defect Engineering, *Adv. Energy Mater.*, 2017, **7**(12), 1602251.
58 Y. Ishida, L. Chabanne, M. Antonietti and M. Shalom, Morphology control and photocatalysis enhancement by the one-pot synthesis of carbon nitride from preorganized hydrogen-bonded supramolecular precursors, *Langmuir*, 2014, **30**(2), 447–451.
59 X.-H. Li, J. Zhang, X. Chen, A. Fischer, A. Thomas, M. Antonietti and X. Wang, Condensed graphitic carbon nitride nanorods by nanoconfinement: promotion of crystallinity on photocatalytic conversion, *Chem. Mater.*, 2011, **23**(19), 4344–4348.
60 W. Wang, J. C. Yu, Z. Shen, D. K. Chan and T. Gu, $g\text{-}C_3N_4$ quantum dots: direct synthesis, upconversion properties and photocatalytic application, *Chem. Commun.*, 2014, **50**(70), 10148–10150.
61 L. Jiang, X. Yuan, Y. Pan, J. Liang, G. Zeng, Z. Wu and H. Wang, Doping of graphitic carbon nitride for photocatalysis: a reveiw, *Appl. Catal., B*, 2017, **217**, 388–406.
62 V. W. Lau, I. Moudrakovski, T. Botari, S. Weinberger, M. B. Mesch, V. Duppel, J. Senker, V. Blum and B. V. Lotsch, Rational design of carbon nitride photocatalysts by identification of cyanamide defects as catalytically relevant sites, *Nat. Commun.*, 2016, **7**, 12165.
63 H. Schlomberg, J. Kröger, G. Savasci, M. W. Terban, S. Bette, I. Moudrakovski, V. Duppel, F. Podjaski, R. Siegel, J. Senker, R. E. Dinnebier, C. Ochsenfeld and B. V. Lotsch, Structural Insights into Poly(Heptazine Imides): A Light-Storing Carbon Nitride Material for Dark Photocatalysis, *Chem. Mater.*, 2019, **31**(18), 7478–7486.
64 R. Godin, Y. Wang, M. A. Zwijnenburg, J. Tang and J. R. Durrant, Time-Resolved Spectroscopic Investigation of Charge Trapping in Carbon Nitrides Photocatalysts for Hydrogen Generation, *J. Am. Chem. Soc.*, 2017, **139**(14), 5216–5224.
65 H. Kasap, C. A. Caputo, B. C. Martindale, R. Godin, V. W. Lau, B. V. Lotsch, J. R. Durrant and E. Reisner, Solar-Driven Reduction of Aqueous Protons Coupled to Selective Alcohol Oxidation with a Carbon Nitride-Molecular Ni Catalyst System, *J. Am. Chem. Soc.*, 2016, **138**(29), 9183–9192.
66 W. Yang, R. Godin, H. Kasap, B. Moss, Y. Dong, S. A. J. Hillman, L. Steier, E. Reisner and J. R. Durrant, Electron Accumulation Induces Efficiency Bottleneck for Hydrogen Production in Carbon Nitride Photocatalysts, *J. Am. Chem. Soc.*, 2019, **141**(28), 11219–11229.
67 G. Zhang, G. Li, Z. A. Lan, L. Lin, A. Savateev, T. Heil, S. Zafeiratos, X. Wang and M. Antonietti, Optimizing optical absorption, exciton dissociation, and charge transfer of a polymeric carbon nitride with ultrahigh solar hydrogen production activity, *Angew. Chem.*, 2017, **129**(43), 13630–13634.
68 G. Zhang, A. Savateev, Y. Zhao, L. Li and M. Antonietti, Advancing the $n \rightarrow \pi^*$ electron transition of carbon nitride nanotubes for H_2 photosynthesis, *J. Mater. Chem. A*, 2017, **5**(25), 12723–12728.
69 A. Savateev, N. V. Tarakina, V. Strauss, T. Hussain, K. Ten Brummelhuis, J. M. Sánchez Vadillo, Y. Markushyna, S. Mazzanti, A. P. Tyutyunnik, R. Walczak, M. Oschatz, D. M. Guldi, A. Karton and M. Antonietti, Potassium Poly(Heptazine Imide): Transition Metal-Free Solid-State Triplet Sensitizer in Cascade Energy Transfer and [3+2]-cycloadditions, *Angew. Chem., Int. Ed.*, 2020, **59**(35), 15061–15068.
70 P. Niu, L. C. Yin, Y. Q. Yang, G. Liu and H. M. Cheng, Increasing the visible light absorption of graphitic carbon nitride (Melon) photocatalysts by homogeneous self-modification with nitrogen vacancies, *Adv. Mater.*, 2014, **26**(47), 8046–8052.
71 Y. Chen, B. Wang, S. Lin, Y. Zhang and X. Wang, Activation of $n \rightarrow \pi^*$ transitions in two-dimensional conjugated polymers for visible light photocatalysis, *J. Phys. Chem. C*, 2014, **118**(51), 29981–29989.
72 F.-Y. Su, C.-Q. Xu, Y.-X. Yu and W.-D. Zhang, Carbon self-doping induced activation of $n\text{-}\pi^*$ electronic transitions of $g\text{-}C_3N_4$ nanosheets for efficient photocatalytic H_2 evolution, *ChemCatChem*, 2016, **8**(22), 3527–3535.
73 J. Xue, M. Fujitsuka and T. Majima, The role of nitrogen defects in graphitic carbon nitride for visible-light-driven hydrogen evolution, *Phys. Chem. Chem. Phys.*, 2019, **21**(5), 2318–2324.
74 L. M. Azofra, D. R. MacFarlane and C. Sun, A DFT study of planar *vs.* corrugated graphene-like carbon nitride (gC_3N_4) and its role in the catalytic performance of CO_2 conversion, *Phys. Chem. Chem. Phys.*, 2016, **18**(27), 18507–18514.
75 N. Ullah, S. Chen, Y. Zhao and R. Zhang, Photoinduced Water-Heptazine Electron-Driven Proton Transfer: Perspective for Water Splitting with g-C, *J. Phys. Chem. Lett.*, 2019, **10**(15), 4310–4316.
76 H. Ma, X. Zhang, F. Jin, H. Zhou, J. Zhang and Y. Ma, Crucial roles of triazinic-N═O and C═O groups in photocatalytic water splitting on graphitic carbon nitride, *J. Mater. Chem. A*, 2021, **9**(9), 5522–5532.
77 P. You, C. Lian, D. Chen, J. Xu, C. Zhang, S. Meng and E. Wang, Nonadiabatic Dynamics of Photocatalytic Water Splitting on A Polymeric Semiconductor, *Nano Lett.*, 2021, **21**(15), 6449–6455.
78 W. Wei and T. Jacob, Strong excitonic effects in the optical properties of graphitic carbon nitride $g\text{-}C_3N_4$ from first principles, *Phys. Rev. B: Condens. Matter Mater. Phys.*, 2013, **87**(8), 085202.
79 M. Z. Rahman and C. B. Mullins, Understanding Charge Transport in Carbon Nitride for Enhanced Photocatalytic Solar Fuel Production, *Acc. Chem. Res.*, 2019, **52**(1), 248–257.
80 C. Butchosa, P. Guiglion and M. A. Zwijnenburg, Carbon Nitride Photocatalysts for Water Splitting: A Computational Perspective. *The*, *J. Phys. Chem. C*, 2014, **118**(43), 24833–24842.
81 K. Srinivasu, B. Modak and S. K. Ghosh, Porous graphitic carbon nitride: a possible metal-free photocatalyst for water splitting, *J. Phys. Chem. C*, 2014, **118**(46), 26479–26484.

82 S. Melissen, Le Bahers, T. Steinmann and S. N. Sautet, P., Relationship between carbon nitride structure and exciton binding energies: a DFT perspective. *The*, *J. Phys. Chem. C*, 2015, **119**(45), 25188–25196.
83 N. Liu, T. Li, Z. Zhao, J. Liu, X. Luo, X. Yuan, K. Luo, J. He, D. Yu and Y. Zhao, From Triazine to Heptazine: Origin of Graphitic Carbon Nitride as a Photocatalyst, *ACS Omega*, 2020, **5**(21), 12557–12567.
84 W. Domcke, A. L. Sobolewski and C. W. Schlenker, Photooxidation of water with heptazine-based molecular photocatalysts: Insights from spectroscopy and computational chemistry, *J. Chem. Phys.*, 2020, **153**(10), 100902.
85 W. Domcke, J. Ehrmaier and A. L. Sobolewski, Solar Energy Harvesting with Carbon Nitrides and N-Heterocyclic Frameworks: Do We Understand the Mechanism?, *ChemPhotoChem*, 2019, **3**(1), 10–23.
86 P. Audebert, E. Kroke, C. Posern and S. H. Lee, State of the Art in the Preparation and Properties of Molecular Monomeric, *Chem. Rev.*, 2021, **121**(4), 2515–2544.
87 C. Merschjann, T. Tyborski, S. Orthmann, F. Yang, K. Schwarzburg, M. Lublow, M.-C. Lux-Steiner and T. Schedel-Niedrig, Photophysics of polymeric carbon nitride: An optical quasimonomer, *Phys. Rev. B: Condens. Matter Mater. Phys.*, 2013, **87**(20), 205204.
88 J. Ehrmaier, T. N. V. Karsili, A. L. Sobolewski and W. Domcke, Mechanism of Photocatalytic Water Splitting with Graphitic Carbon Nitride: Photochemistry of the Heptazine-Water Complex, *J. Phys. Chem. A*, 2017, **121**(25), 4754–4764.
89 C. W. Schlenker and M. E. Thompson, The molecular nature of photovoltage losses in organic solar cells, *Chem. Commun.*, 2011, **47**(13), 3702–3716.
90 G. Ren, C. W. Schlenker, E. Ahmed, S. Subramaniyan, S. Olthof, A. Kahn, D. S. Ginger and S. A. Jenekhe, Photoinduced hole transfer becomes suppressed with diminished driving force in polymer–fullerene solar cells while electron transfer remains active, *Adv. Funct. Mater.*, 2013, **23**(10), 1238–1249.
91 E. J. Rabe and C. W. Schlenker, Excited-state Energies Drive Charge-transfer in Organic Semiconductors. In *World Scientific Handbook of ORGANIC OPTOELECTRONIC DEVICES: Organic Photovoltaics (OPVs)*, World Scientific, Volume 2, 2018, pp. 89–120.
92 D. A. Armstrong, R. E. Huie, W. H. Koppenol, S. V. Lymar, G. Merényi, P. Neta, B. Ruscic, D. M. Stanbury, S. Steenken and P. Wardman, Standard electrode potentials involving radicals in aqueous solution: inorganic radicals (IUPAC Technical Report), *Pure Appl. Chem.*, 2015, **87**(11–12), 1139–1150.
93 E. J. Rabe, K. L. Corp, X. Huang, J. Ehrmaier, R. G. Flores, S. L. Estes, A. L. Sobolewski, W. Domcke and C. W. Schlenker, Barrierless Heptazine-Driven Excited State Proton-Coupled Electron Transfer: Implications for Controlling Photochemistry of Carbon Nitrides and Aza-Arenes, *J. Phys. Chem. C*, 2019, **123**(49), 29580–29588.
94 V. Viswanathan, H. A. Hansen and J. K. Nørskov, Selective Electrochemical Generation of Hydrogen Peroxide from Water Oxidation, *J. Phys. Chem. Lett.*, 2015, **6**(21), 4224–4228.
95 S. Siahrostami, G. L. Li, V. Viswanathan and J. K. Nørskov, One- or Two-Electron Water Oxidation, Hydroxyl Radical, or H, *J. Phys. Chem. Lett.*, 2017, **8**(6), 1157–1160.
96 X. Shi, S. Siahrostami, G. L. Li, Y. Zhang, P. Chakthranont, F. Studt, T. F. Jaramillo, X. Zheng and J. K. Nørskov, Understanding activity trends in electrochemical water oxidation to form hydrogen peroxide, *Nat. Commun.*, 2017, **8**(1), 701.
97 J. H. Baek, T. M. Gill, H. Abroshan, S. Park, X. Shi, J. Nørskov, H. S. Jung, S. Siahrostami and X. Zheng, Selective and Efficient Gd-Doped $BiVO_4$ Photoanode for Two-Electron Water Oxidation to H_2O_2, *ACS Energy Lett.*, 2019, **4**(3), 720–728.
98 F. Weber, J. C. Tremblay and A. Bande, Proton-Coupled Electron-Transfer Dynamics of Water Oxidation at N-Doped Graphene Oxides, *J. Phys. Chem. C*, 2020, **124**(49), 26688–26698.
99 A. L. Sobolewski and W. Domcke, Photoinduced water splitting with oxotitanium porphyrin: a computational study, *Phys. Chem. Chem. Phys.*, 2012, **14**(37), 12807–12817.
100 K. Yamamoto and K. Takatsuka, On the photocatalytic cycle of water splitting with small manganese oxides and the roles of water clusters as direct sources of oxygen molecules, *Phys. Chem. Chem. Phys.*, 2018, **20**(9), 6708–6725.
101 X. Li, G. Hartley, A. J. Ward, P. A. Young, A. F. Masters and T. Maschmeyer, Hydrogenated defects in graphitic carbon nitride nanosheets for improved photocatalytic hydrogen evolution, *J. Phys. Chem. C*, 2015, **119**(27), 14938–14946.
102 K. L. Corp and C. W. Schlenker, Ultrafast Spectroscopy Reveals Electron-Transfer Cascade That Improves Hydrogen Evolution with Carbon Nitride Photocatalysts, *J. Am. Chem. Soc.*, 2017, **139**(23), 7904–7912.
103 A. Köhler and H. Bässler, *Electronic processes in organic semiconductors: An introduction*. John Wiley & Sons: 2015.
104 C. Ruckebusch, M. Sliwa, P. D. Pernot, A. De Juan and R. Tauler, Comprehensive data analysis of femtosecond transient absorption spectra: A review, *J. Photochem. Photobiol., C*, 2012, **13**(1), 1–27.
105 J. Snellenburg, S. Laptenok, R. Seger, K. Mullen and I. Van Stokkum, *Glotaran: A Java-based graphical user interface for the R package TIMP*, 2012.
106 Y. Wang, X. Wang and M. Antonietti, Polymeric graphitic carbon nitride as a heterogeneous organocatalyst: from photochemistry to multipurpose catalysis to sustainable chemistry, *Angew. Chem., Int. Ed.*, 2012, **51**(1), 68–89.
107 X. L. Wang, W. Q. Fang, W. Liu, Y. Jia, D. Jing, Y. Wang, L.-Y. Yang, X.-Q. Gong, Y.-F. Yao and H. G. Yang, Brønsted base site engineering of graphitic carbon nitride for enhanced photocatalytic activity, *J. Mater. Chem. A*, 2017, **5**(36), 19227–19236.
108 P. Niu, M. Qiao, Y. Li, L. Huang and T. Zhai, Distinctive defects engineering in graphitic carbon nitride for greatly extended visible light photocatalytic hydrogen evolution, *Nano Energy*, 2018, **44**, 73–81.
109 C. Wang, Q. Wan, J. Cheng, S. Lin, A. Savateev, M. Antonietti and X. Wang, Efficient aerobic oxidation of alcohols to esters by acidified carbon nitride photocatalysts, *J. Catal.*, 2021, **393**, 116–125.
110 V. W. Lau, M. B. Mesch, V. Duppel, V. Blum, J. Senker and B. V. Lotsch, Low-molecular-weight carbon nitrides for solar hydrogen evolution, *J. Am. Chem. Soc.*, 2015, **137**(3), 1064–1072.
111 S. Kumar, N. Sharma and K. Kailasam, Emergence of *s*-heptazines: from trichloro-*s*-heptazine building blocks to functional materials, *J. Mater. Chem. A*, 2018, **6**(44), 21719–21728.
112 J.-F. Zheng, Z.-P. Xie, Z. Li, Y. Chen, X. Fang, X. Chen and M.-J. Lin, Structural design of small-molecule carbon-nitride dyes for photocatalytic hydrogen evolution, *Dyes Pigm.*, 2021, **185**, 108946.
113 E. J. Rabe, K. L. Corp, A. L. Sobolewski, W. Domcke and C. W. Schlenker, Proton-Coupled Electron Transfer from Water to a Model Heptazine-Based Molecular Photocatalyst, *J. Phys. Chem. Lett.*, 2018, **9**(21), 6257–6261.
114 S. R. Flom and P. F. Barbara, Proton transfer and hydrogen bonding in the internal conversion of S1 anthraquinones, *J. Phys. Chem.*, 1985, **89**(21), 4489–4494.
115 G. R. Han, D. Hwang, S. Lee, J. W. Lee, E. Lim, J. Heo and S. K. Kim, Shedding new light on an old molecule: quinophthalone displays uncommon N-to-O excited state intramolecular proton transfer (ESIPT) between photobases, *Sci. Rep.*, 2017, **7**(1), 3863.
116 J. Liu, Y. Liu, N. Liu, Y. Han, X. Zhang, H. Huang, Y. Lifshitz, S.-T. Lee, J. Zhong and Z. Kang, Metal-free efficient photocatalyst for stable visible water splitting via a two-electron pathway, *Science*, 2015, **347**(6225), 970–974.
117 K. L. Corp, E. J. Rabe, X. Huang, J. Ehrmaier, M. E. Kaiser, A. L. Sobolewski, W. Domcke and C. W. Schlenker, Control of Excited-State Proton-Coupled Electron Transfer by Ultrafast Pump–Push–Probe Spectroscopy in Heptazine–Phenol Complexes: Implications for Photochemical Water Oxidation, *J. Phys. Chem. C*, 2020, **124**(17), 9151–9160.
118 P. Dongare, A. G. Bonn, S. Maji and L. Hammarström, Analysis of Hydrogen-Bonding Effects on Excited-State Proton-Coupled Electron Transfer from a Series of Phenols to a Re(I) Polypyridyl Complex, *J. Phys. Chem. C*, 2017, **121**(23), 12569–12576.
119 J. R. Lakowicz, *Principles of fluorescence spectroscopy*. Springer science & business media, 2013.
120 E. J. Rabe, H. J. Goldwyn, D. Hwang, D. J. Masiello and C. W. Schlenker, Intermolecular Hydrogen Bonding Tunes Vibronic Coupling in Heptazine Complexes, *J. Phys. Chem. B*, 2020, **124**(51), 11680–11689.
121 C. Bronner and O. S. Wenger, Kinetic isotope effects in reductive excited-state quenching of Ru (2,2′-bipyrazine) 32+ by phenols. *The*, *J. Phys. Chem. Lett.*, 2012, **3**(1), 70–74.
122 M. Yamaji, J. Oshima and M. Hidaka, Verification of the electron/proton coupled mechanism for phenolic H-atom transfer using a triplet π, π* carbonyl, *Chem. Phys. Lett.*, 2009, **475**(4-6), 235–239.
123 J. J. Warren, T. A. Tronic and J. M. Mayer, Thermochemistry of proton-coupled electron transfer reagents and its implications, *Chem. Rev.*, 2010, **110**(12), 6961–7001.

124 M. de Jong, L. Seijo, A. Meijerink and F. T. Rabouw, Resolving the ambiguity in the relation between Stokes shift and Huang-Rhys parameter, *Phys. Chem. Chem. Phys.*, 2015, **17**(26), 16959–16969.
125 H. Baessler and B. Schweitzer, Site-selective fluorescence spectroscopy of conjugated polymers and oligomers, *Acc. Chem. Res.*, 1999, **32**(2), 173–182.
126 K. Huang and A. Rhys, Theory of light absorption and non-radiative transitions in F-centres, *Proc. R. Soc. London, Ser. A*, 1950, **204**(1078), 406–423.
127 C. Hansch, A. Leo and R. Taft, A survey of Hammett substituent constants and resonance and field parameters, *Chem. Rev.*, 1991, **91**(2), 165–195.
128 Y. H. Liu, S. M. Wang, C. W. Wang, C. Zhu, K. L. Han and S. H. Lin, Orientation hydrogen-bonding effect on vibronic spectra of isoquinoline in water solvent: Franck-Condon simulation and interpretation, *J. Chem. Phys.*, 2016, **145**(16), 164314.
129 X. Yan, H. Zhang, W. Cai, A. Zhao, J. Wang and W. Shen, Effects of intramolecular hydrogen bonds on phosphorescence emission: A theoretical perspective, *Appl. Organomet. Chem.*, 2020, **34**(4), e5527.
130 M. Dierksen and S. Grimme, Density functional calculations of the vibronic structure of electronic absorption spectra, *J. Chem. Phys.*, 2004, **120**(8), 3544–3554.
131 D. Karpovich and G. Blanchard, Relating the polarity-dependent fluorescence response of pyrene to vibronic coupling. Achieving a fundamental understanding of the py polarity scale, *J. Phys. Chem.*, 1995, **99**(12), 3951–3958.
132 H. Mustroph and A. Towns, Fine Structure in Electronic Spectra of Cyanine Dyes: Are Sub-Bands Largely Determined by a Dominant Vibration or a Collection of Singly Excited Vibrations?, *ChemPhysChem*, 2018, **19**(9), 1016–1023.
133 X. Liu, A. L. Sobolewski, R. Borrelli and W. Domcke, Computational investigation of the photoinduced homolytic dissociation of water in the pyridine–water complex, *Phys. Chem. Chem. Phys.*, 2013, **15**(16), 5957–5966.
134 J. Ehrmaier, M. J. Janicki, A. L. Sobolewski and W. Domcke, Mechanism of photocatalytic water splitting with triazine-based carbon nitrides: insights from *ab initio* calculations for the triazine–water complex, *Phys. Chem. Chem. Phys.*, 2018, **20**(21), 14420–14430.
135 X. Liu, T. N. Karsili, A. L. Sobolewski and W. Domcke, Photocatalytic Water Splitting with the Acridine Chromophore: A Computational Study, *J. Phys. Chem. B*, 2015, **119**(33), 10664–10672.
136 A. A. Bakulin, A. Rao, V. G. Pavelyev, P. H. van Loosdrecht, M. S. Pshenichnikov, D. Niedzialek, J. Cornil, D. Beljonne and R. H. Friend, The role of driving energy and delocalized States for charge separation in organic semiconductors, *Science*, 2012, **335**(6074), 1340–1344.
137 T. W. Kee and Femtosecond Pump-Push-Probe, and Pump-Dump-Probe Spectroscopy of Conjugated Polymers: New Insight and Opportunities, *J. Phys. Chem. Lett.*, 2014, **5**(18), 3231–3240.
138 S. S. Lim, D. Giovanni, Q. Zhang, A. Solanki, N. F. Jamaludin, J. W. M. Lim, N. Mathews, S. Mhaisalkar, M. S. Pshenichnikov and T. C. Sum, Hot carrier extraction in CH, *Sci. Adv.*, 2019, **5**(11), eaax3620.
139 S. Lin, H. Huang, T. Ma and Y. Zhang, Photocatalytic Oxygen Evolution from Water Splitting, *Adv. Sci.*, 2020, 2002458.
140 V. Balzani, L. Moggi, M. F. Manfrin, F. Bolletta and M. Gleria, Solar Energy Conversion by Water Photodissociation: transition metal complexes can provide low-energy cyclic systems for catalytic photodissociation of water, *Science*, 1975, **189**(4206), 852–856.
141 Y. Nosaka and A. Nosaka, Understanding hydroxyl radical (•OH) generation processes in photocatalysis, *ACS Energy Lett.*, 2016, **1**(2), 356–359.
142 A. C. Maier, E. H. Iglebaek and M. Jonsson, Confirming the formation of hydroxyl radicals in the catalytic decomposition of H_2O_2 on metal oxides using coumarin as a probe, *ChemCatChem*, 2019, **11**(22), 5435–5438.
143 J. Ehrmaier, E. J. Rabe, S. R. Pristash, K. L. Corp, C. W. Schlenker, A. L. Sobolewski and W. Domcke, Singlet-Triplet Inversion in Heptazine and in Polymeric Carbon Nitrides, *J. Phys. Chem. A*, 2019, **123**(38), 8099–8108.
144 H. Kollmar and V. Staemmler, Violation of Hund's rule by spin polarization in molecules, *Theor. Chim. Acta*, 1978, **48**(3), 223–239.
145 S. Koseki, T. Nakajima and A. Toyota, Violation of Hund's multiplicity rule in the electronically excited states of conjugated hydrocarbons, *Can. J. Chem.*, 1985, **63**(7), 1572–1579.
146 R. Englman and J. Jortner, The energy gap law for radiationless transitions in large molecules, *Mol. Phys.*, 1970, **18**(2), 145–164.
147 J. Ehrmaier, X. Huang, E. J. Rabe, K. L. Corp, C. W. Schlenker, A. L. Sobolewski and W. Domcke, Molecular Design of Heptazine-Based Photocatalysts: Effect of Substituents on Photocatalytic Efficiency and Photostability, *J. Phys. Chem. A*, 2020, **124**(19), 3698–3710.
148 S. Samanta and R. Srivastava, Catalytic conversion of CO_2 to chemicals and fuels: the collective thermocatalytic/photocatalytic/electrocatalytic approach with graphitic carbon nitride, *Mater. Adv.*, 2020, **1**(6), 1506–1545.
149 R. Liu, Z. Chen, Y. Yao, Y. Li, W. A. Cheema, D. Wang and S. Zhu, Recent advancements in gC_3N_4-based photocatalysts for photocatalytic CO_2 reduction: a mini review, *RSC Adv.*, 2020, **10**(49), 29408–29418.
150 Q. Lu, K. Eid, W. Li, A. M. Abdullah, G. Xu and R. S. Varma, Engineering Graphitic Carbon Nitride (g-C_3N_4) for Catalytic Reduction of CO_2 to Fuels and Chemicals: Strategy and Mechanism, *Green Chem.*, 2021, **23**(15), 5394–5428.
151 J. Ehrmaier, A. L. Sobolewski and W. Domcke, Role of the pyridinyl radical in the light-driven reduction of carbon dioxide: a first-principles study, *J. Phys. Chem. A*, 2019, **123**(17), 3678–3684.
152 J. Qin, S. Wang, H. Ren, Y. Hou and X. Wang, Photocatalytic reduction of CO_2 by graphitic carbon nitride polymers derived from urea and barbituric acid, *Appl. Catal., B*, 2015, **179**, 1–8.
153 J. Fu, B. Zhu, C. Jiang, B. Cheng, W. You and J. Yu, Hierarchical porous O-doped g-C_3N_4 with enhanced photocatalytic CO_2 reduction activity, *Small*, 2017, **13**(15), 1603938.
154 P. Yang, H. Zhuzhang, R. Wang, W. Lin and X. Wang, Carbon vacancies in a melon polymeric matrix promote photocatalytic carbon dioxide conversion, *Angew. Chem., Int. Ed.*, 2019, **58**(4), 1134–1137.
155 H. Li, B. Zhu, S. Cao and J. Yu, Controlling defects in crystalline carbon nitride to optimize photocatalytic CO_2 reduction, *Chem. Commun.*, 2020, **56**(42), 5641–5644.
156 X. Zheng, P. Yu and J. Wang, Ultrafast intramolecular vibrational energy transfer in carbon nitride hydrocolloid examined by femtosecond two-dimensional infrared spectroscopy, *J. Chem. Phys.*, 2019, **150**(19), 194703.
157 M. J. Muñoz-Batista, M. A. Nasalevich, T. J. Savenije, F. Kapteijn, J. Gascon, A. Kubacka and M. Fernández-García, Enhancing promoting effects in g-C_3N_4-Mn +/CeO_2-TiO_2 ternary composites: Photo-handling of charge carriers, *Appl. Catal., B*, 2015, **176**, 687–698.
158 M. D. Capobianco, B. Pattengale, J. Neu and C. A. Schmuttenmaer, Single Copper Atoms Enhance Photoconductivity in g-C_3N_4, *J. Phys. Chem. Lett.*, 2020, **11**(20), 8873–8879.